Sustainable Energy & Fuels

Beyond Conventional Batteries: A Review on Semi-Solid and Redox Targeting Flow Batteries-LiFePO4 as a Case Study

Journal:	*Sustainable Energy & Fuels*
Manuscript ID	SE-REV-01-2024-000064.R1
Article Type:	Review Article
Date Submitted by the Author:	29-Feb-2024
Complete List of Authors:	El Halya, Nabil; Mohammed VI Polytechnic University Tayoury, Marwa; Mohammed VI Polytechnic University Aqil, Mohamed; Mohammed VI Polytechnic University Aboulaich, Abedelhay; Mohammed VI Polytechnic University Amine, Rachid; University of Illinois at Chicago, Chemical Engineering; Argonne National Laboratory, Materials Science Division Ghamouss, Fouad; Mohammed VI Polytechnic University, Department of Materials Science, Energy, and nano-Engineering; Makha, Mohammed; Mohammed VI Polytechnic University Alami, Jones; Mohammed VI Polytechnic University, MSN Dahbi, Mouad; Mohammed VI Polytechnic University,

ARTICLE

Beyond Conventional Batteries: A Review on Semi-Solid and Redox Targeting Flow Batteries-$LiFePO_4$ as a Case Study

Received 00th January 20xx,
Accepted 00th January 20xx

DOI: 10.1039/x0xx00000x

Nabil El Halya[a], Marwa Tayoury[a], Mohamed Aqil[a], Abedelhay Aboulaich[a], Rachid Amine[b], Fouad Ghamouss[a], Mohammed Makha[a], Jones Alami[a], and Mouad Dahbi[a]*

Abstract

Clean and sustainable energy is becoming increasingly crucial to tackle the current energy crisis. However, the intermittent nature of renewable energy sources presents a challenge for their effective implementation. Redox flow batteries (RFBs) have emerged as a promising solution to this problem, as they can help enhance the stability of grid networks and promote the use of renewable energy sources. RFBs are highly modular and scalable systems that can be customized to meet the power and energy requirements of different renewable energy plants. Moreover, they offer several advantages over conventional battery technologies, including cost and safety concerns. However, conventional RFBs have limited energy densities due to the low solubility of their active species in electrolyte. To overcome this limitation, semi-solid (SSRFBs) and Redox targeting (RTFBs) flow batteries have been proposed. These systems feature high concentrations of active species and impressive energy densities, making them highly attractive for renewable energy applications. $LiFePO_4$ (LFP) is a highly promising active material for Semi-Solid and Targeting Flow Batteries. One of the key advantages of LFP is its low raw materials cost, as it is composed of earth-abundant elements such as iron and phosphorus. This makes it an attractive option for large-scale battery production. The recent developments in SSRFBs and RTFBs using $LiFePO_4$ as catholyte hold great promise for the future of sustainable energy storage. The combination of LFP's excellent cost, safety, durability, and high energy density with the modularity and scalability of flow battery systems make for a compelling solution to the challenges of intermittent renewable energy sources. Ongoing research and development in this area will likely yield even further improvements in the performance and efficiency of LFP-based flow batteries, opening exciting new possibilities for sustainable energy storage.

1. Introduction

Clean and sustainable energy presents a viable solution to the energy crisis we face today. However, relying solely on solar farms and wind turbines may not suffice to yield substantial benefits to society and the environment. The progress in this field is subject to the uncertain and intermittent characteristics of renewable energy sources. To promote the utilization of renewable and sustainable energy and also enhance the stability of grid networks, energy storage systems are needed to store excess electricity. [1–6] For this reason, flow batteries have been developed. This flexible and modular process can be scaled very precisely according to the power and energy requirements of a renewable energy plant. Moreover, redox flow batteries have great advantages comparing with other types of batteries such as low cost, high safety and quick response. [7–10] The principle of redox flow batteries (RFBs) is based on oxidation/reduction reactions at each of the electrodes. The specificity of this technology comes from the fact that the reagents are in solution in a different electrolyte for the anode and cathode, they are therefore stored in two separate tanks and circulate in two half-cells. The two reagents are separated by a semi-permeable membrane which allows the passage of ions to ensure the electroneutrality of the cell. Pumps ensure the circulation of the electrolytes in order to renew each reagent on the surface of the corresponding electrode. [11–13]

Vanadium Redox Flow batteries are considered the most reliable systems. In fact, they don't suffer from the mixing of the electrolytes (cross-contamination) since they have the same vanadium in the catholyte and anolyte. As a result, this system possesses a long cycling life. So, this technology has a great potential for large scale stationary storage. Unfortunately, this battery still suffers from the low energy density comparing to conventional lithium-ion batteries. The reason behind this problem is the low stability of vanadium ions in a certain temperature as well as the low concentration of vanadium that can be dissolved in the supporting electrolyte (less than 2M). This concentration corresponds to an energy density of 25 Wh kg^{-1} or 33 Wh L^{-1}. [11,14–16]

The low solubility of active species of vanadium in electrolyte limits its energy density. To overcome this problem, the semi-solid flow batteries with impressive energy densities and high concentration of active species were proposed by a research team from MIT University.[17,18] In fact, this technology consists of active material particles with conductive additives suspended in liquid electrolyte for both positive (catholyte) and negative (anolyte) electrode. The active suspensions are stored in two energy storage reservoirs and pumped into the electrochemical cell during charge/discharge processes. This hybrid design offers the advantage of flexibility of flow batteries and the high energy density of lithium-ion batteries. However, the poor fluidity and high viscosity of the suspension creates a significant barrier for practical operation. For this, another approach which consists in pumping only the liquid phase, leaving the solid active materials in the energy storage tanks has

[a]*Materials Science and Nano-engineering Department, Mohammed VI Polytechnic University, Ben Guerir, Morocco*
[b]*Materials Science Division, Argonne National Laboratory, 9700 S. Cass Avenue Lemont, IL 60439, USA*

been proposed. This technology named redox targeting flow battery consists of organic or organo-metallic molecules dissolved in the electrolyte as mediators between the electrodes in the electrochemical cell and the solid materials in the tanks. Soluble mediators with redox potentials targeting those of the solid active materials are necessarily needed for the oxidation and reduction reactions. By keeping solid materials in the tanks, only the liquid electrolyte containing the redox mediators is being pumped.[19–22]

The first semi-solid system was proposed by chiang and coworks using $LiCoO_2$ as catholyte and $Li_4Ti_5O_{12}$ as anolyte in carbonate electrolyte.[17] This concept combines the advantage of high energy density of lithium-ion batteries and the decoupled power and energy of Redox Flow Batteries. The energy density of the battery was estimated to be 300-500 Wh L^{-1} (130-250 Wh kg^{-1}). Chiang and his group were also optimized the ratio of the different particles in the slurry.[23] Other works done by Craig Carter et al. were studied the fluidity of the suspension using simulation methods [24] as well as Franco and coworkers were used a model to understand the charge-discharge behavior of the semi-solid flow batteries.[25] Moreover, other works were conducted to evaluate the effect of the diffusion and dynamics of the material suspension on the performance of the battery.[26] Recently, Edgar Ventosa et al. used $Na_xNi_{0.22}Co_{0.11}Mn_{0.66}O_2$ and $NaTi_2(PO_4)_3$ as catholyte and anolyte, respectively, for a non-aqueous system.[27] The Semi-Solid Flow Batteries were applied also in aqueous electrolyte. In fact, Chiang et al. evaluated the $LiFePO_4$ catholyte and $LiTi_2(PO_4)_3$ in $LiNO_3$ aqueous electrolyte.[28] In the case of Targeting Redox Flow Batteries, several works were done using different electroactive materials with a variety of mediators. In 2013, Huang et al. proposed a targeting system using $LiFePO_4$ (3.45 V vs. Li^+/Li) as cathode with ferrocene (3.25 vs. Li^+/Li)) and dibromoferrocene (3.65 V vs. Li^+/Li) as shuttle molecules As well as TiO_2 (1.80 V vs. Li^+/Li) as anode and cobaltocene (1.95 V vs. Li^+/Li) and bis(pentamethylcyclopentadienyl)cobalt (1.36 V vs. Li^+/Li) as mediators.[29] Moreover, Huang et al suggested a lithium-iodide redox flow lithium battery, which consists of a lithium anode and an iodide catholyte with $LiFePO_4$ as the energy storage material.[30] In another study, $LiFePO_4$ with a bi-functional redox mediator 2,3,5,6 tetramethyl-p-phenylenediamine (TMPD) was proposed by Guang Zhu et al.[31]

One of the key challenges of semi-solid and redox targeting flow batteries is improving their energy density and power density. This can be achieved by optimizing the design of the RFB, developing new electrolytes, and improving the performance of the electrodes. Another challenge is to increase the efficiency of the battery. This can be achieved by reducing the resistance of the electrolyte and improving the charge and discharge rates. In addition, the use of advanced materials, such as nanomaterials, may also help to improve the efficiency of the battery. In this context, $LiFePO_4$ is among the promising cathodes, which are extensively studied in Lithium-ion batteries due to its low cost, low toxicity, high chemical/thermal stability and high specific capacity (170 $mAhg^{-1}$).[32–34] However, the sluggish diffusion kinetics of lithium ions and the poor electronic conductivity, resulting in a significant capacity loss at high C-rate, are the main obstacles that limit the performances of this material. Several strategies have been developed to overcome the aforementioned issues such as particle size reduction,[35–37] surface coating,[38–41] preparation of composite electrodes,[42–44] addition of conductive binders,[45–47] and doping.[48–51] All these strategies have shown encouraging results in lithium-ion batteries, but less attention has been given to the application of these advanced $LiFePO_4$ based materials for redox flow batteries. The development of LFP with advanced morphological and electronic properties could be a good direction to improve the performance of LFP based RFBs. In the case of SSRFBs, the use of $LiFePO_4$ with optimized morphological properties, such as a high surface area and uniform particle size, can further irove the performance of the battery by increasing the electrode/electrolyte interface area and reducing mass transfer limitations. Moreover, in the case of RTFBs, the use of $LiFePO_4$ with optimized electronic properties, such as high conductivity and low resistance, can improve the efficiency and power output of RTFBs. In this review, we will summarize the different studies interested in the application of $LiFePO_4$ as catholyte for Redox Flow Batteries.

2. Basics on the Redox flow batteries

The main differences between redox flow and conventional batteries are the dynamic nature of the electrolytes, the decoupled energy and power. In this section, a detailed description of the working principle, configuration and key components of redox flow technology will be presented.

2.1. Redox flow batteries Vs Other batteries

In conventional batteries, the energy is stored in the active materials of the electrodes. However, in Redox Flow Batteries, the energy and active materials are stored in liquid electrolytes which can circulate between the electrolyte reservoirs and the electrochemical cell using peristaltic pumps. Consequently, Redox Flow Batteries have some unique characteristics. [52–54]

- In the case of conventional batteries, power and energy are not fully decoupled. In fact, the energy density can be increased by increasing the thickness of the electrodes, but it is limited by the power. However, in the case of Redox Flow Batteries, the energy can be increased simply by increasing the number of electrolyte tanks and the concentration of active species in the electrolyte. Furthermore, the power can be increased by varying the configuration of the electrochemical cell.
- Redox Flow Batteries possess high Coulombic efficiencies due to the high electrochemical reversibility of the dissolved active species in the electrolytes.
- Compared to other batteries, Redox Flow Batteries have much longer lifetime which can be estimated at over 10000 cycles for 10-20 years. This high lifetime can be explained by the stability of electrodes which do not contribute to the redox reactions, as well as by the internal structural stability of the soluble active species. Redox Flow Batteries have other features such as the good deep-discharge capability, mild operational temperatures, and safety etc.

2.2. Working principle

In redox flow battery technology, the energy storage materials are liquid (anolyte and catholyte) stored in two external reservoirs. During the battery operation, the electrolytes circulate via a pumping system through a cell compartments containing cathodic and anodic current collectors separated by an ion-selective membrane (Figure. 1). The redox reactions of the active materials take place on the surface of the current collectors, and the charge balance of the cell is ensured by the transport of the anion and/or cation of the supporting electrolyte through the ionic selective membrane. The positive active species undergo an oxidation reaction and lose electrons during the charge, whereas the negative active species undergo a reduction reaction receiving electrons from the external circuit. The opposite reactions occur during the discharge process.

2.3. Key components

2.3.1. Active materials

In RFBs, the active materials are the crucial components that determine the electrochemical performance of the battery. In fact, these active materials should have some features such as high electrolyte solubility to deliver high capacity, high electrochemical reversibility to ensure high columbic efficiency, and appropriate redox potential to achieve high energy density. The electrolyte is composed of active material, solvent and supporting electrolyte to increase the ion conductivity.

Table 1 The main characteristics, advantages and disadvantages of storage technologies.[55]

	Power density	Advantages	Disadvantages
Lead Acid Battery	30-50 Wh/kg	Low cost; high effeciency; High recycled content	Low energy density; Short lifetime
Sodium-Sulfur Battery	150-250 Wh/kg	High energy density; High effeciency; Long lifetime	High initial cost; Safety issues
Lithium-Ion Battery	200 Wh/kg	High energy density; High effeciency; Long lifetime; Environmentally friendly.	Short lifetime and elevated cost in large scale such as grid applications
Vanadium Redox Flow Battery	16-33 Wh/kg	High effeciency; Long lifetime; Environmentally friendly.	Low energy density; Risk of cross contamination of electrolyte

2.3.2. Membrane

The primary role of the membrane is the separation of the catholyte and anolyte and ensuring the charge balance of the cell via its ionic selectivity, which allows specific ions to pass to the other side and block the others. When choosing a membrane for RFB application, chemical and mechanical stability, ionic conductivity and selectivity as well as cost must be taken into consideration. For these reasons, ion exchange and porous membrane can be used.[56–64]

2.3.3. Electrodes

In Redox Flow Batteries, the electrodes do not have any participation in the electrochemical reactions, but they have an important role in the catalysis of these reactions via their high active surface area. In general, carbon paper, carbon felt, and graphite are the most used materials due to their high porosity and specific surface area.[65–72]

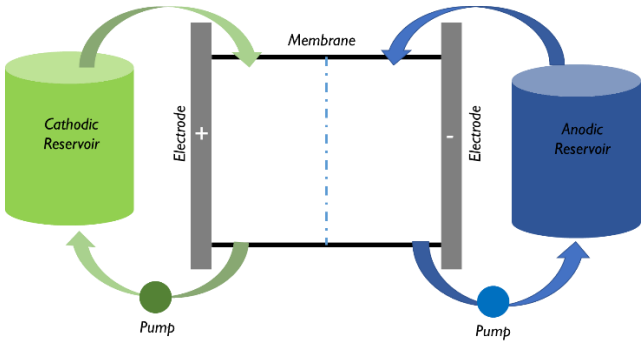

Figure. 1 Scheme of a redox flow battery.

3. Types of Redox Flow Battery technology

In the past decades, different types of RFBs were developed. On the basis of the nature of the redox materials and cell design. RFBs can be divided into metal based RFBs, Organic based RFBs, Polymer based RFBs, Hybrid RFBs, Solar rechargeable RFBs, Semi-Solid Redox Flow Batteries and redox-targeting flow batteries. In this section, we discuss the advantages and challenges of each type of RFBs.

3.1. Metal based RFBs

After the invention of the first RFB (iron-chromium RFB) by Thallet at NASA in 1974, different RFBs were developed based on metallic active species as catholyte and anolyte. Among existing metal based RFBs, iron-titanium,[73] all vanadium,[74–80] iron-vanadium,[68,81–83] vanadium-bromine,[84,85] vanadium-cerium,[86–89] etc have been developed. Some of these systems are used today on an industrial scale such as all vanadium RFB developed by Skyllas–Kazacos in 1980s, considered as the most commercially successful RFB system nowadays.

3.2. Organic based RFBs

Despite the wide commercial adoption of metal based RFBs, they still suffer from several drawbacks such as the limited energy density, low solubility and the high cost of active species. In this context, the development of inexpensive and sustainable organic active species can solve the aforementioned problems. The redox active molecules can be easily extracted from nature. However, they must present certain characteristics such as high stability and the good reversibility. Several aqueous and non-aqueous organic RFBs have been developed since 2011, nevertheless, further studies must be conducted to enhance energy density as well as the cycling stability.[90–103]

3.3. Polymer based RFBs

The need for an expensive Nafion ion exchange membrane for common RFBs has prompted scientists to research for other active materials that allow the use of cost-effective exclusion / dialysis membranes and microporous separators. For this reason, polymers with high molecular weight have been proposed as catholyte and anolyte for RFBs. The first polymers reported as charge storage materials were polyaniline (PANI), poly (vinylbenzylethylviologene) and 2,2,6,6-tetramethylpiperidin-1-oxyl (TEMPO), this opened the door to further develop new high-performance polymers for RFBs application.[18,104–113]

3.4. Hybrid RFBs

Replacing liquid electrolytes with metals appears to be a good approach to increase the energy density of RFBs due to the higher energy density and the simple redox chemistry of metals. A Hybrid RFB, with half-cell reaction, is based on the deposition of solid species. Various Hybrid RFBs exist in the literature which including Zinc and lithium-based hybrid flow batteries. For the Zinc based hybrid flow batteries, the most known system is the zinc–bromine battery with an experimental specific energy of 65–75 $Whkg^{-1}$.[114] However, for the Lithium-based hybrid flow batteries, the most developed systems are the Lithium-iodide battery with an energy density of 550 WhL^{-1} (300 $Whkg^{-1}$), and the Lithium-polysulfide battery with an energy density which could be up to 108 WhL^{-1} (97 $Whkg^{-1}$), with 5.0 M polysulfide electrolyte.[114–120]

3.5. Solar rechargeable RFBs

In recent years, an interesting development of RFBs is their integration with photoelectrochemical cells, to store solar energy as chemical energy. In fact, in a solar flow battery, the redox active species can be directly charged by solar radiation using semi-conductor photoelectrodes, before being discharged to generate electricity. Despite the huge interest in this technology, it still suffers from low power conversion efficiencies, which is an obstacle for large scale applications.[121–130]

3.6. Semi-Solid Redox Flow Batteries (SSRFBs)

To overcome the problem of limited energy density of conventional RFBs due to the low solubility of active species, Semi-solid flow battery (SSFB) was proposed by Chiang et al. in 2011.[17] In this technology, the catholyte and anolyte contain a suspension of Li insertion materials, conductive additives (Ketjen black) and aqueous or non-aqueous electrolyte. During operation of the battery, the suspensions circulate via a pumping system between the tanks and the cell stack containing the electrodes for the electrochemical reactions, and the polymer membrane to prevent the crossover of negative and positive active materials. Several lithium insertion materials have been tested in this technology and encouraging energy densities have been achieved. For example, the $LiCoO_2$–$Li_4Ti_{15}O_{12}$ couple with a cell voltage of 2.35 V showed an energy density of 397 WhL^{-1}, and $LiCoO_2$-graphite couple with a cell voltage of 3.8 V reached an energy density of 615 WhL^{-1}. [17,131–140]

3.7. Redox Targeting Flow Batteries (RTFBs)

Using semi-solid technology, high concentration of active species and enhanced energy density can be achieved. However, the high viscosity of the suspension and the need of expensive conductive additives present big obstacle for practical operation. To overcome the problems of SSRFBs, the redox targeting technology has been proposed by Wang et al. in 2006. In fact, in this system, the solid active materials used in conventional Li-ion batteries remain statically in external tanks containing redox electrolytes with suitable redox molecules. During the battery operation, the redox molecules circulate by pumping between the tanks and the cell stack containing the electrodes. The chemical reaction between the redox molecules and the solid active material takes place in the external tank, while the electrochemical reaction between the redox molecules and the electrode takes place in cell stack. The capacity of the battery is determined by the capacity of the active materials, but not by the dissolved redox molecules.[141,142] Several lithium insertion materials have been tested as catholyte and anolyte for targeting RFB such as LFP, $NaV_2(PO_4)_3$, TiO_2, etc.[143–152]

Among all the technologies available, Semi-Solid (SSFBs) and Redox Targeting Flow Batteries (RTFBs) are interesting approaches to enhance the energy density of Redox Flow Batteries. These technologies overcome the solubility limit of redox species by using lithium-ion battery materials in the form of flowable slurry (Fig. 1a, b) or static in the reservoirs (Fig. 1c, d). As shown in Fig. 2a, the most developed vanadium technology has an energy density that does not exceed 30 Wh/Kg. However, SSRFBs and RTFBs have the potential to deliver an energy density of up to 300 Wh/kg (Fig. 2a). Despite their attractive energy densities, these technologies have received less attention, as shown in Fig. 2b, where the publication number for these two technologies in 2023 does not exceed 2% of the total number of publications in the field of Redox Flow Batteries. This review aims to shed lighter on these promising technologies. Moreover, because of the huge interest given to $LiFePO_4$ (LFP) as an energy storage material thanks to its several advantages such as the low raw materials cost (earth-abundant elements (Fe and P)), safety, durability, and good energy density, we will focus on the various works in which LFP is used as catholyte for SSRFBs and RTRFBs.

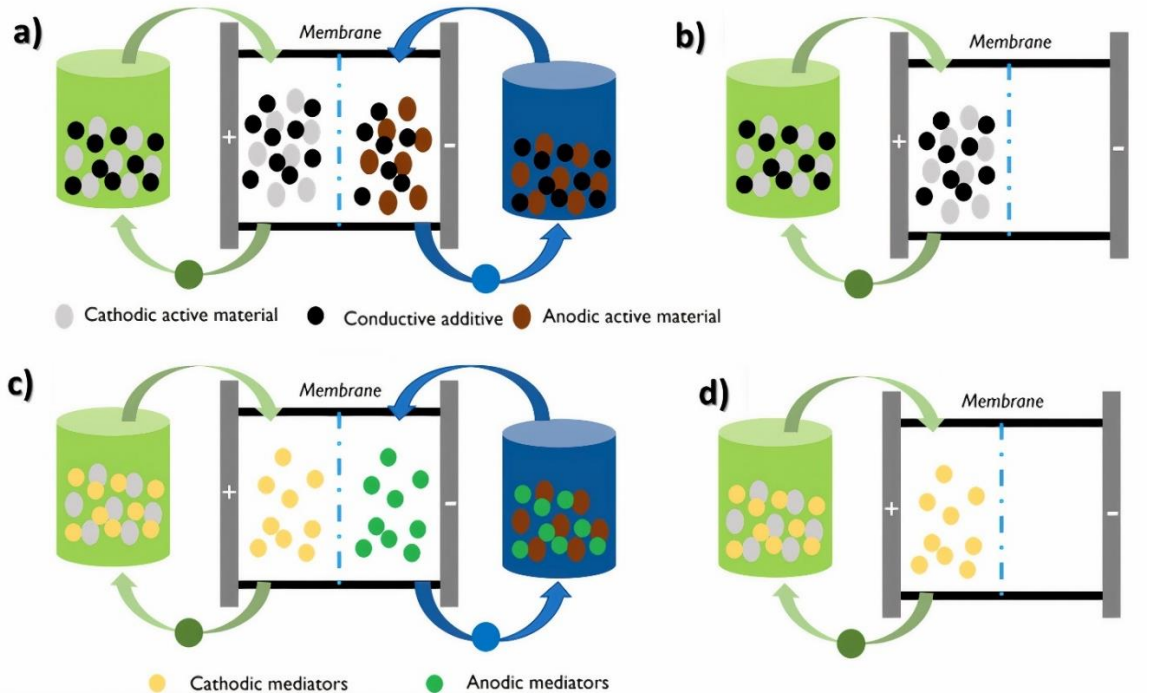

Fig. 1 Configuration of (a) Full cell Semi Solid Redox flow battery, (b) hybrid Semi Solid Redox flow battery, (c) Full cell Redox targeting flow battery, (d) hybrid Redox targeting flow battery.

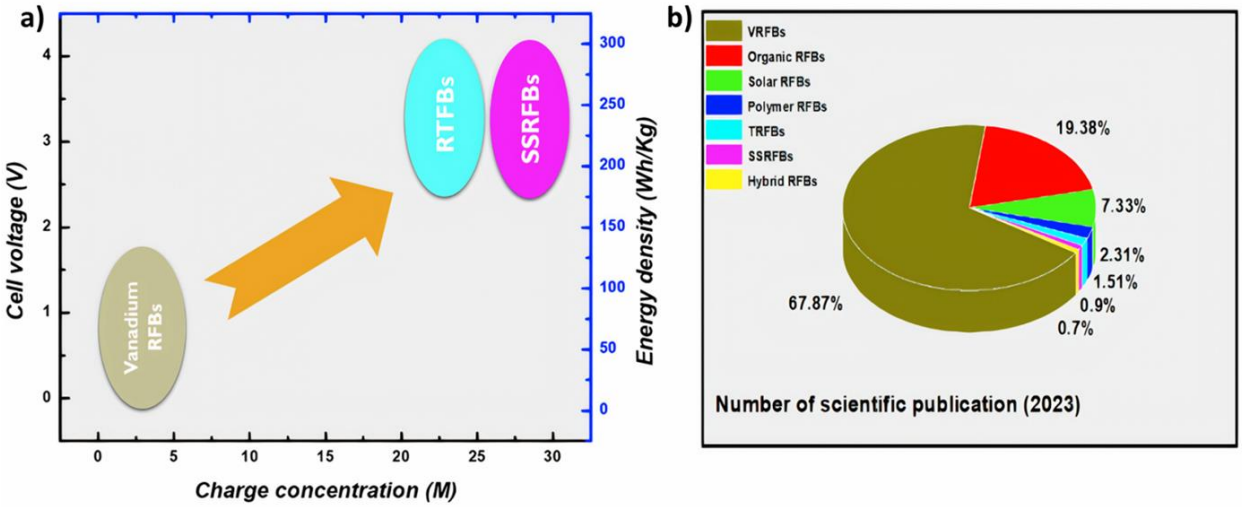

Fig. 2 (a) Cell voltage, Charge concentration and Energy density of Vanadium (VRFB), Semi-Solid (SSRFB) and Redox targeting Redox Flow Battery (RTRFB). (b) Number of scientific publications for different Redox Flow Battery technologies using Scopus as the publication database.

4. $LiFePO_4$ Based Semi-Solid Redox Flow Lithium-ion Batteries

4.1. LFP slurry-based flow battery with Zn anode

To improve the energy density (Wh L^{-1}) of Redox flow batteries (RFB) it is necessary to increase the cell voltage or the volumetric capacity. The first solution is limited by the electrochemical stability window of the aqueous solvent which does not exceed 1.5 V. Consequently, enhancing the volumetric capacity is the efficient route to solve this problem of aqueous systems. For this reason, various strategies have been proposed such as the use of a high-energy metal electrode, the development of active species with high solubility or the use of high energy intercalation materials as semi-solid electrodes. In this context, Edgar Ventosa et al proposed a novel concept of high-energy redox flow batteries based on coupling semi-solid electrodes with high-energy Zn metal electrodes, in a mixed cation aqueous electrolyte.[153] In this type of concepts, the "rocking-chair" principle is not respected because the concentration of cations varies with the state of charge.[154,155] Consequently, the concentration of Zn^{2+} ions decrease, and that of Li^{+} ions increase during the charge/discharge process. This concept can be feasible in flow batteries. However, the high viscosity of slurries with high content of active material is the limiting factor due to the low flowability. As a result, the energy density of semi-solid flow batteries dependent on the content of the positive electrode in the catholyte and its operating potential. In this work, the Edgar Ventosa's group has tested commercially C-coated $LiFePO_4$ material as solid electrode with Zn metal as counter electrode in 1 M $ZnSO_4$/0.2 M Li_2SO_4 aqueous solution (Fig.3a).[153] $LiFePO_4$ was revealed satisfying reversibility in the prepared electrolyte with an operating potential of 1.2 V vs Zn/Zn^{2+}, and a specific capacity of 90-100 mAh g^{-1} at 1C confirming the previous reports.[156,157] Fig. 3b present the galvanostatic measurements of the slurry containing 12 wt % $LiFePO_4$ and 1.5 wt % Ketjenblack. The results showed excellent electrochemical reversibility and a specific capacity of 140 mAh g^{-1}. Besides, the Coulombic efficiency was >99% confirming the good selectivity, and the capability of the separator to minimize the crossing of the active material (the pore size of Celgard 3501 is 0.064 µm, while the particle size of the commercial $LiFPO_4$ is between 0.210 and 18 µm). As in most Zn-based batteries, the Cyclability of this system needs to be improved (Fig. 3c).[158] Fig. 3d prove the full utilization of $LiFePO_4$ (140 mAh g^{-1}) under continuous flow, and the energy density was increased from 25 to 50 WhL^{-1} when the content of $LiFePO_4$ was increased from 12 wt % to 22 wt %. These results confirmed the proportionally relationship between the energy density and the content of active material. This proof of concept proved its capability to operate at 16 mA cm^{-2} under continuous flow (Fig. 3e) but could not operate efficiently at higher current densities.

To increase the operating current density as well as the voltage efficiency, the use of 3D current collector for the negative electrode and more slurry optimization are needed. Moreover, the optimization and comprehension of semi-solid electrodes in aqueous media are predicted to increase the battery performances, such as voltage efficiency and energy density. More importantly, to compete with current and developed battery technologies, the cyclability of Zn electrodes in neutral environments needs to be improved. In general, the Zn-semi-solid hybrid-flow batteries are more suitable for stationary energy storage applications with constrained area. Higher energy densities might be obtained by replacing Zn by other metals such as Al which could open the door for a wider range of applications.

ARTICLE

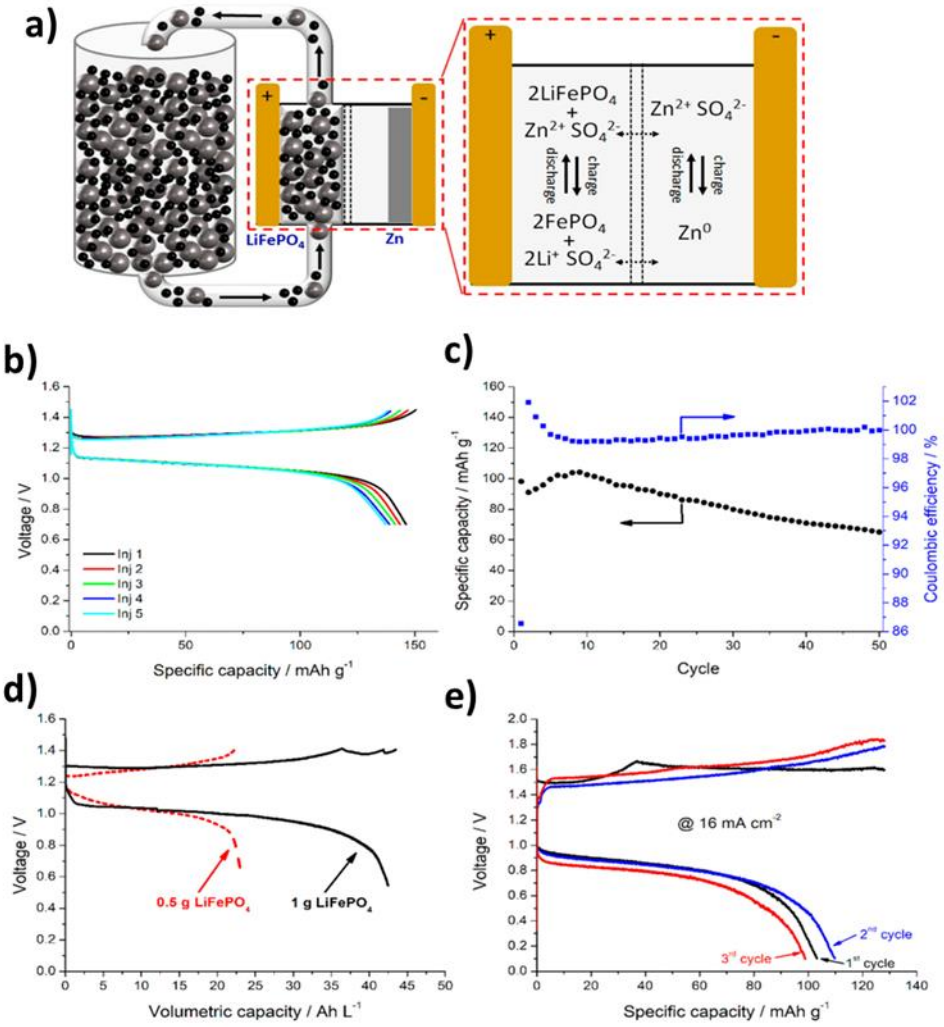

Fig. 3 Schematic illustration of aqueous Zn–semi-solid hybrid-flow batteries, along with a description of the electrochemical processes occurring at the negative and positive electrodes during the charging and discharging (a) Galvanostatic measurements of a Zn–$LiFePO_4$ hybrid-flow battery in (b, c) static mode and (d, e) continuous flow. Reproduced from ref. 149 with permission from American Chemical Society, Copyright 2018.

4.2. LFP slurry-based flow battery with 3D current collector

To reduce the viscosity and improve the energy density of the active slurry, Hongning Chen et al. have demonstrated a single component concept slurry-based lithium-ion flow battery with a 3D current collector (Fig. a, b).[159] The advantages of the proposed flow lithium-ion battery are as follows:

- Low viscosity
- Improved volumetric capacity and energy density due to the high-volume ratio of active materials.
- High interaction between the electrochemically active slurry and the 3D current collector with large surface area.

Fig. 4c present the cyclic voltammetry tests of 10 vol% $LiFePO_4$ with different current collectors. The result shows reversible redox reaction of LFP at ~3.45 V vs. Li/Li^+ for Carbon Cloth (CC), Carbon Felt (CF) and Carbon Paper (CP) current collectors. Moreover, the CF provide larger peak current (1.62 mA) in comparison with CC (1.35 mA) and CP (1.14 mA). This result is proved by EIS results, which show lower charge transfer resistance for CF (Fig. 4d). The reason behind this result could be attributed to the porous structure and large pore size of CF, which plays a role in improving the contact between the LFP suspension and the surface of the current collector. In addition, Fig. 4e shows a linear relationship between oxidation/reduction peak currents and square root of the scanning rates, which signifies that the redox reactions of LFP slurry are under the control of lithium ion diffusion. The first charge/discharge cycles of 10 vol% $LiFePO_4$ slurry with different 3D current collectors are

presented in Fig. 4f. The highest specific capacity is achieved with CF current collector (134 mAh/g) compared with CC and CP (120 and 97 mAh/g respectively). This result also confirms the beneficial effect of CF 3D current collector over CC and CP. Fig. 4g shows the first cycles of the galvanostatic charge/ discharge tests of 10 vol% $LiFePO_4$ slurry at different C-rates (0.2-1C) using CF current collector. The first specific capacity at 0.2C was 134 mAh g^{-1}, and that at 1C was 101 mAh g^{-1}, which is comparable to the results obtained from LFP solid electrode in lithium-ion batteries. Besides, the cycling performance (Fig. 4h) shows the higher capacity retention of the cell with CF current collector (82% after 100 cycles), compared of those of CC (59%) and CP (53%). A volumetric capacity of 68 Ah L^{-1}, with a concentration of active material in the slurry of 40% was achieved in this work using $LiFePO_4$ (LFP) with a 3D carbon felt stream. The energy density was 230 Wh L^{-1} with a coulombic efficiency of 95% over 100 cycles in a coin cell, and improved stability in flow-cell tests.

This study demonstrated the success of a single-component slurry flow battery with 3D current collectors with improved energy density. This concept may provide a new opportunity and possibilities for future optimization on 3D porous current collectors, as well as the practical fraction of active materials to maximize the volumetric capacity and minimize viscosity. Moreover, the current and power density can still be much improved. One strategy is to give LFP particles a more homogeneous carbon coating to increase their electrical conductivity. Better rate performance would also result from changing the flow cell design's geometrical structure (such as decreasing the electrode's thickness) and creating new porous current collectors with strong electrical conductivity and the proper pore structure. With these advancements, it is anticipated that the proposed single-component slurry-based lithium-ion flow battery's power density will be significantly increased, and its energy density will exceed that of conventional all-vanadium and iron-chromium flow batteries.

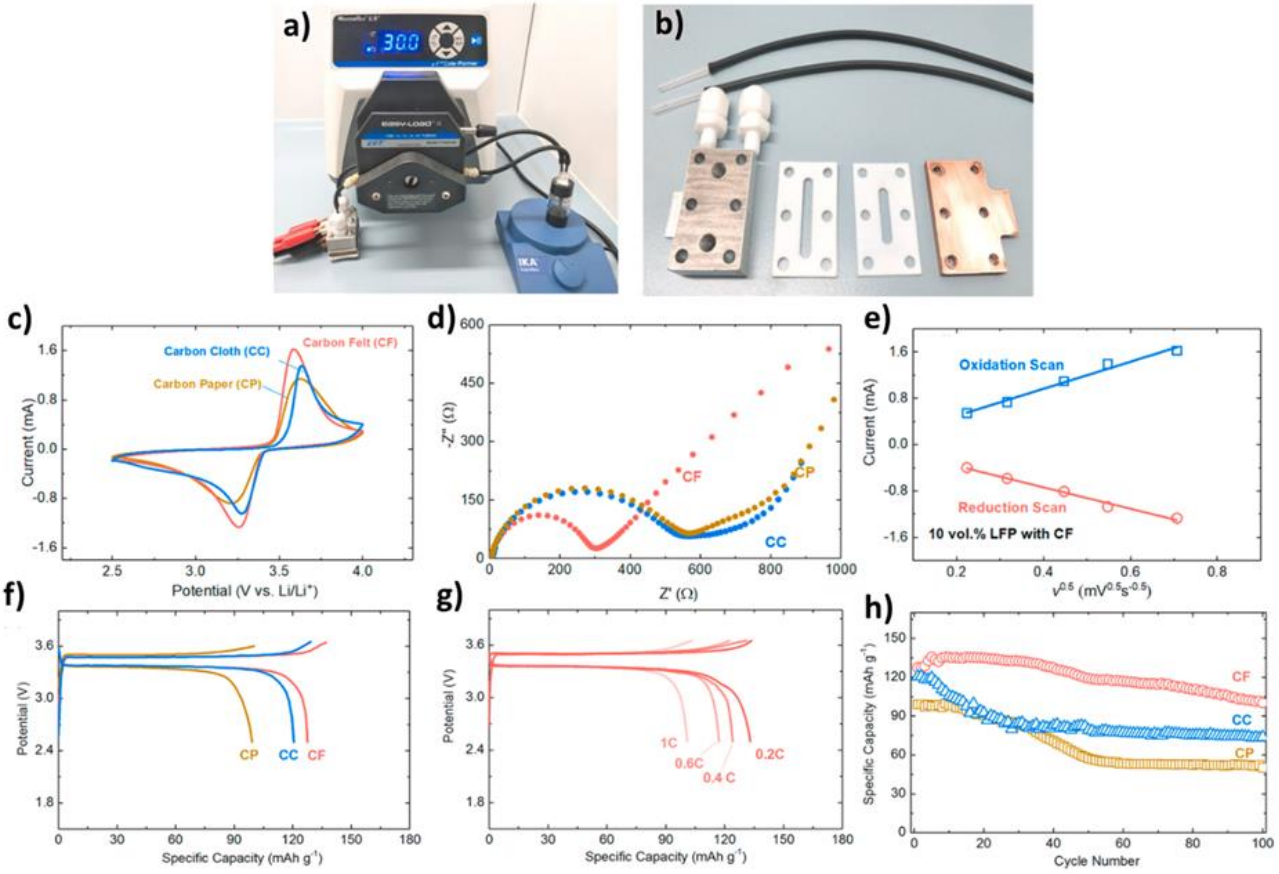

Fig. 4 (c) Cyclic Voltammograms of LFP slurry with different current collectors in static cell (d) EIS measurements of LFP slurry with different current collectors (e) Peak currents as a function of square root of scanning rates for LFP slurry (f) First charge-discharge cycles of LFP slurry at 0.2C (g) First charge-discharge cycles of LFP slurry with CF at various C-rates (h) Cycling performances of LFP slurry at 0.2C. Reproduced from ref. 155 with permission from Elsevier, Copyright 2021.

4.3. LFP slurry-based flow battery with Carbon Nanotubes (CNTs)

Recently, Yansong luo et al. proposed a solution to address the high viscosity of the suspensions for SSFBs, which is primarily caused by the percolating conductor network, results in significant pump dissipations.[44] The study suggests synthesizing LFP active material together with carbon nanotubes (CNTs) to accelerate the electrons and ions transfer and reduce the impact of the percolating network on suspensions' viscosities. The LFP/CNT composites were synthesized through sol-gel method using various CNT contents. Three suspensions known as Suspension LFP/5CNTs, LFP/10CNTs, and LFP/15CNTs were studied.

According to Fig. 5 (a-c), the electrochemical impedance of the suspensions is largely dominated by the measured charge transfer resistances. The electrochemical impedances of all the suspensions decrease as conductive additive amounts rise. The CNTs-based suspensions have the lowest electrochemical impedance, and the charge transfer resistance of the Suspension LFP/5CNTs and the Suspension LFP/15CNTs is nearly identical to

that of the KB-based suspensions. Overall, the LFP/15CNTs-based slurry exhibits a comparatively low viscosity and a low electrochemical impedance. Using the modified Swagelok cell, the charge and discharge tests (Fig. 5d) were carried out using several LFP/CNT-based suspensions. The obtained initial charge specific capacities LFP/5CNTs, LFP/10CNTs, and LFP/15CNTs are 66 mAh g^{-1}, 89 mAh g^{-1}, and 116 mAh g^{-1}, respectively. Therefore, the estimated energy densities for the cell with Suspended LFP/5CNTs, LFP/10CNTs, and LFP/15CNTs, respectively, are 22 $Whkg^{-1}$, 30 $Whkg^{-1}$, and 36 $Whkg^{-1}$. The obtained results show that the LFP/15CNTs-based suspension is the optimal formulation due to its high charge specific capacity and high charge transport properties. Moreover, the LFP/15CNTs-based suspensions demonstrates best performances comparing to the commercial LFP-based suspension in terms of charge transport capability, and charge/discharge properties (Fig.5e and f).

Although the LFP/CNTs composites-based suspensions present low viscosity and high charge transport properties, more optimizations must be done especially the parameters of the synthesis process such as the temperature, the time of the reaction and calcination conditions to further improve the electrochemical performances. Additionally, LFP/CNT composites-based suspensions must be studied in flow mode to evaluate the cycle performance of the suspensions.

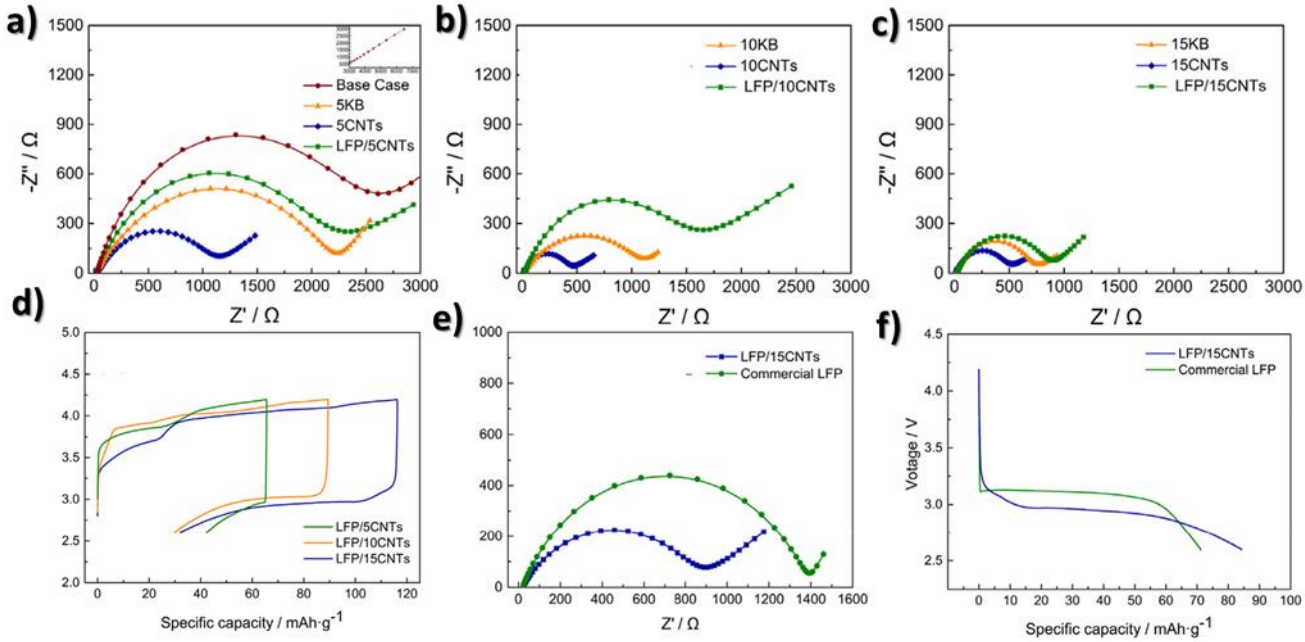

Fig. 5 (a, b, c) electrochemical impedance spectra, expressed by Nyquist plots for commonly-used suspensions and LFP/CNTs-based suspensions for Li-ion SSFBs with different volume of conductive additives. (d) Charge and discharge profiles of LFP/ CNTs-based suspensions within the potential region from 2.6 to 4.2 V. (e, f) electrochemical impedance and initial discharge capacity of the Suspension LFP/15CNTs and the Suspension Commercial LFP. Reproduced from ref. 42 with permission from Elsevier, Copyright 2023.

4.4. Fire hazard of the electrolyte and slurries used for LFP based SSRFBs

To study the fire hazard of the electrolyte and slurries used for SSRFBs, Qiangling Duan et al. performed a series of combustion experiments on electrolytes and slurries using cone calorimeter.[160] The first part of the study compares the combustion properties of the electrolytes containing different lithium source ($LiPF_6$ and LiTFSI). A series of TG-DTG tests were carried out to better understand the combustion behavior of various electrolytes. The Heat Release Rate (HRR) of a mixture of electrolytes and solvents had the following orders: EC/DMC EC/DMC > $LiPF_6$ > EC/DMC LiTFSI. While the pHRR of the LiTFSI-based electrolyte was much lower than that of the solvent combination, it was marginally higher for the $LiPF_6$-based electrolyte. LiTFSI-based electrolytes have a pHRR that is 30.3% lower than $LiPF_6$-based electrolytes. The second section of the study focuses on the fire risk of the slurry. Several electrode materials ($Li_4Ti_5O_{12}$, $LiNi_{0.8}Co_{0.1}Mn_{0.1}O_2$, $LiFePO_4$, and Graphite) were studied to identify the combustion properties of electrode slurries. The order of the pHRR of the various slurries is as follows: S-LTO > S-LFP > S-NCM > S-Graphite. S-LTO and S-LFP exhibit larger pHRRs than S-NCM and S-Graphite due to the intense splashing during combustion. Moreover, the CO release rate curves of all slurries (with the exception of S-LTO) are comparable to that of the electrolytes. The rate of CO emission was modest in the early stages of combustion but dramatically rose in the final stages. In contrast to the electrolyte, the CO generation rate curve of S-LTO had two equivalent peaks caused by the ferocious splash which may promote the propagation of fire.

The bursting of the bubbles produced inside the slurry at the slurry-air interface may be the cause of the slurry splashing. The vaporization of the low-boiling component (DMC) of the combined solvents inside the slurry following overheating and the high-temperature gas-generating reaction between the electrolyte and the electrode material are the two potential causes of bubble formation. Yet, splashing is not always present when bubbles occur. Many variables, including the gas flux as well as the slurry's characteristics like viscosity, surface tension, thermal conductivity, etc., may affect splashing's occurrence and intensity. Moreover, the inclusion of various electrode materials alters these slurry properties to varying degrees, which eventually results in variations in the splashing intensity of various slurries. Ultimately, further research must be done on the intricate mechanism of splashing.

4.5. LFP slurry-based flow battery with Nafion/PVDF/LLZTO ion exchange membrane

One of the key challenges in the development of SSRFBs is maintaining the cycling stability of the battery over many charge-discharge cycles. The low cycling stability is caused by the high permeability of the active components through the porous separator. This can lead to cross-contamination of the electrodes, which can reduce the efficiency of the battery and shorten its lifetime. Another challenge is the low conductivity of lithium ions in non-porous membranes, which limits the overall performance of the battery. To address these challenges, Ruji Wang et al. proposed a novel ion exchange membrane (IEM) made from a blend of Nafion, PVDF, and LLZTO ($La_{0.3}Li_{0.2}Zr_{0.533}Ta_{0.067}O_3$), which has high ion conductivity and mechanical properties.[161] The resulting Nafion/PVDF/LLZTO IEM showed a high ionic

conductivity (3 wt% LLZTO demonstrates a maximum ionic conductivity up to 0.29 mS cm^{-1}). It also had good mechanical properties, including high tensile strength and flexibility, which make it suitable for use in a flow battery. The cross-sectional SEM image of sandwich-like membrane is depicted in Fig. 6a. It is apparent from the image that the upper and lower layers are upheld by Celgard PE, which acts as a protector for effective safeguarding. The functional ingredient, NPL3 coating interlayer, with a thickness of 30 µm, is attached to PE membrane without any delamination.

The cycling tests showed that the battery with the new IEM presents better stability and efficiency at 0.1C after 80 cycles when using LFP as cathode and lithium metal as anode (Fig. 6b). Moreover, excellent stability and rate capability were obtained when using this membrane in a full cell configuration (LFP as cathode and LTO as anode) compared to a battery with a traditional Nafion membrane (Fig. 6c). To evaluate the performance of the prepared composite membrane in slurry cell, a slurry pouch cells was assembled, and the result is depicted in Fig. 6d. LFP//LTO semi-solid system employing PE/NPL3/PE membrane delivers excellent initial capacity of 0.7mAh·cm^{-2} at 0.3 C with high-capacity retention of 71.4% after 120 cycles. Besides, PE/NPL3/PE membrane was used in a slurry flow reactor composed from LFP slurry in one side and lithium metal in the other side (Fig.7e). Fig. 7f shows the cycling performance under static mode at 0.25 mA cm -2. The system exhibits a capacity of 210 µAh with stable coulombic efficiency of 89% after 14 cycles. Fig. 6g presents the charge/discharge voltage plateaus which corresponds to the redox activity of LFP. Despite the few cycles, these initial results show the promising performance of the PE/NPL3/PE sandwich-like structure membrane.

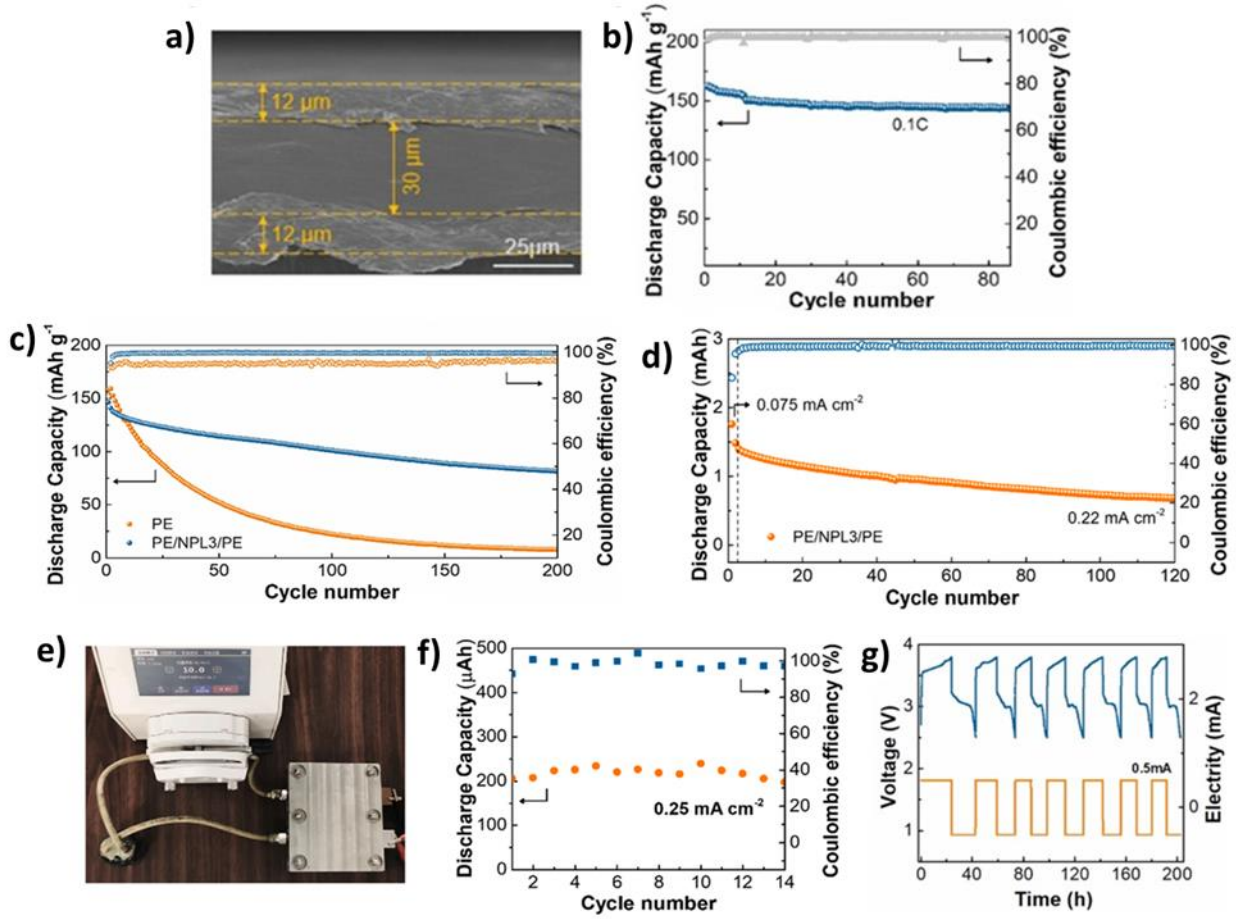

Fig. 6 (a) Cross-sectional SEM image of PE/NPL3/PE membrane. (b) Cycling of $LiFePO_4$//PE/NPL3/PE//Li cells at 0.1 C. (c) Cycle performance of LFP//LTO cells with different membranes at 0.3 C. (d) Cycle performance with Coulombic efficiency at 0.22 mA cm^{-2} of PE/NPL3/PE in semi-solid LFP//LTO pouch cell. (e) Digital photograph of the assembled slurry flow cell in test state. (f) Cycle performance of the flow cell under and (g) the corresponding voltage profiles. Reproduced from ref. 157 with permission from Elsevier, Copyright 2023.

4.6. Injectable LFP battery for more efficient and cost-effective recycling

To make the battery recycling easier, Daniel Perez-Antolin et al. suggested an innovative battery concept based on semi-solid electrodes.[162] Traditional batteries contain binders and active materials that are fixed onto the current collectors. This makes it difficult to recover the active materials for recycling. However, in this innovative battery concept, semi-solid electrodes are used instead. These semi-solid electrodes do not contain any binders and the active materials are not fixed onto the current collectors. This allows for direct recovery of the active materials by dejecting the flowable electrodes from the battery cell. The reuse of the battery cells is also possible in this concept, including all inactive elements such as current collectors, separators, and casing. This simplifies the recycling process by eliminating several steps, leading to significant reductions in the battery cost. Overall, this concept is designed to make battery recycling more efficient and cost-effective (Fig.7a). A mixture of $LiFePO_4$, carbon additive, stabilizer, and electrolyte (78.3 w%, 21.1 w%, and 0.6 w%, respectively) is used to make the semi-solid electrodes shown in Fig. 7b. During the initial cycle, the battery delivred an aerial capacity of 2.5 mAh cm^{-2} and a specific capacity of 130 mAh g^{-1} of $LiFePO_4$ at 1C, as shown in Fig. 7c. Unfortunately, the capacity quickly dropped to 0.2 mAh cm^{-2} after only 50 cycles. Using the overpotentials displayed in Fig. 7c, the internal resistance was estimated, and it was found

to remain relatively constant across the different injections (Fig. 7d). The minor differences in the areal capacity (2.5 ± 0.25 mA h cm^{-2}) observed between regenerations were attributed to the reproducibility of the homemade regeneration process, as there was no discernible trend over the course of the five injections. This suggests that the idea of battery regeneration/recycling through the straightforward replacement of the semi-solid electrode is possible.

The use of super-concentrated electrolytes (21 m LiTFSI and 1 m ZnTFSI) in this injectable battery resulted in a significant increase in cycle stability compared to the standard electrolyte. After 300 cycles, the capacity retention values for the super-concentrated electrolytes were 70%. These findings suggest that the use of super-concentrated electrolytes is a promising approach for reducing side reactions in semi-solid electrodes. Moreover, the concept of an injectable battery was implemented for an aqueous Li-ion battery chemistry, specifically using $LiFePO_4$ – $LiTi_2(PO_4)_3$ (LFP – LTP). In this implementation, both LTP and LFP were used as semi-solid electrodes, delivering a typical nominal voltage of 0.9 V and a specific capacity of 45 mA h g^{-1} LTP. Compared to the Zn – LFP injectable battery, the capacity fading was improved (Fig. 7e and f). The super-concentrated LTP – LFP systems had a coulombic efficiency of over 99% and energy efficiency of over 75%.

Despite the encouraging results of the new concept of injectable battery, the increased porosity of semi-solid electrodes will lead to a penalty for specific and energy density. As a result, it would be beneficial to investigate the injectable battery concept for low-cost battery chemistries that are designed for stationary energy storage purposes.

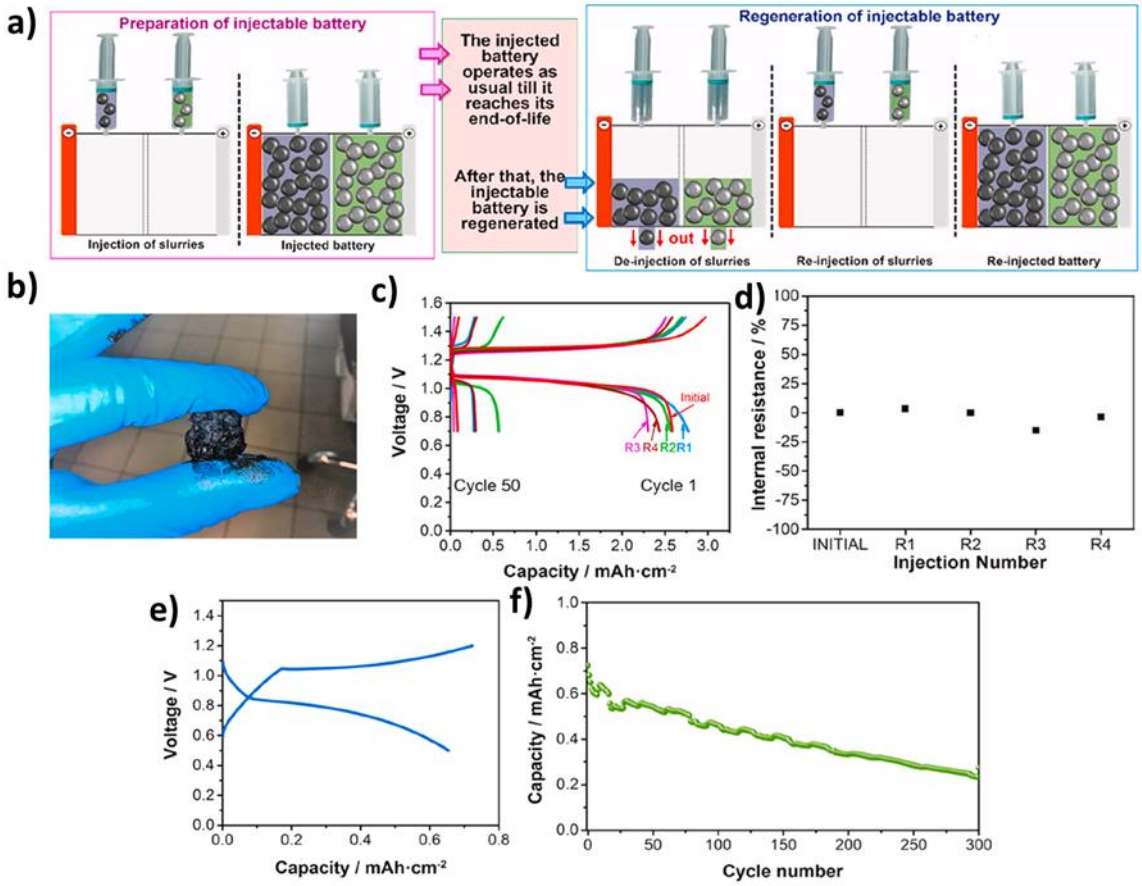

Fig. 7 (a) Illustration of the injectable battery concept. (b) Photograph of a semi-solid electrode. (c) Voltage profile of an injected Zn – $LiFePO_4$ battery in the 1st and 50th cycle for the initial battery and after 4 subsequent regenerations (R1, R2, R3 and R4) at 1C (2.5 mA cm^{-2}). (d) Variation of the internal resistance of the injectable battery with respect to initial value when semi-solid electrodes are substituted. (e, f) Voltage profile and evolution of the areal capacity with cycles for the $LiTi_2(PO_4)_3$ – $LiFePO_4$ injectable battery. Reproduced from ref. 158 with permission from Elsevier, Copyright 2020.

4.7. 3D multi-physics coupled simulation model of LFP based SSRFBs

A comprehensive 3D multi-physics coupled simulation model of SSRFBs is a mathematical tool that allows researchers and engineers to simulate the behavior of SSRFBs under different operating conditions. The model considers various physical phenomena that occur in the battery, including electrochemistry, fluid dynamics, and heat transfer. In this context, Kun Yang et al. proposes a 3D multi-physics coupled simulation model that can accurately describe the dynamic state of charge (SOC) in SSRFBs considering flow convection. The model integrates the transport equations for mass, momentum, and energy in the slurry flow domain with the electrochemical reactions that occur at the electrode surface. Fig. 8a displays the computational meshes and precise dimensions of the flow field.[163]

To determine the accuracy of the proposed model, Kun Yang et al. compared the simulation results with experimental data. Fig. 8b illustrates the comparison between the modeled and measured battery potentials during the initial four charge-discharge cycles. Both charge and discharge cycles were conducted using a current density of 0.5 mA cm^{-2}, with charge-discharge cutoff voltages set at 3.8 V and 2.5 V, respectively. The results indicate that the model accurately predicts the battery potential during charge-discharge cycling. The discrepancy between the simulated and measured voltage platform could be attributed to differences in conductivity description. In practical designs of the SSRFB, the slurry typically flows through fixed channels rather than directly through the electrode surface. The design of these flow channels can have an impact on the performance of the SSRFB, and two common flow field designs were evaluated in this study. The velocity

distribution of the slurry within these two channels is shown in Fig. 8c. The uniformity of velocity distributions in the parallel flow field can result in an increase in charge capacity and Coulombic efficiency. Furthermore, due to the larger flow area in the parallel flow field compared to the serpentine flow field, the pressure drop between the inlet and outlet is reduced. This reduction in pressure drop can significantly decrease pumping losses. Moreover, Fig. 8d reveals that the relationship between pressure drops and flow rate is non-linear, with the pressure drops increasing gradually as the flow rate increases. Additionally, the parallel structure of the flow channel creates a small area with very low flow velocity, known as a "dead zone," which impedes slurry flow. As a result, the flow channel's structural design significantly impacts the behavior of slurry flow and, consequently, influences the performance of SSRFB. Fig. 8e shows the velocity results on the middle cut line of the two flow fields. The slurry displays plug-like flow behavior, with the primary velocity change taking place at the channel's edge. In contrast, the velocity in the channel's middle section remains relatively constant in the crosswind direction, creating a plug-like area.

Overall, a comprehensive 3D multi-physics coupled simulation model of SSRFBs is a powerful tool for understanding the behavior of these complex systems and optimizing their performance. As the demand for renewable energy sources continues to grow, the development of SSRFBs is likely to become increasingly important, and simulation models will play a crucial role in their design and optimization.

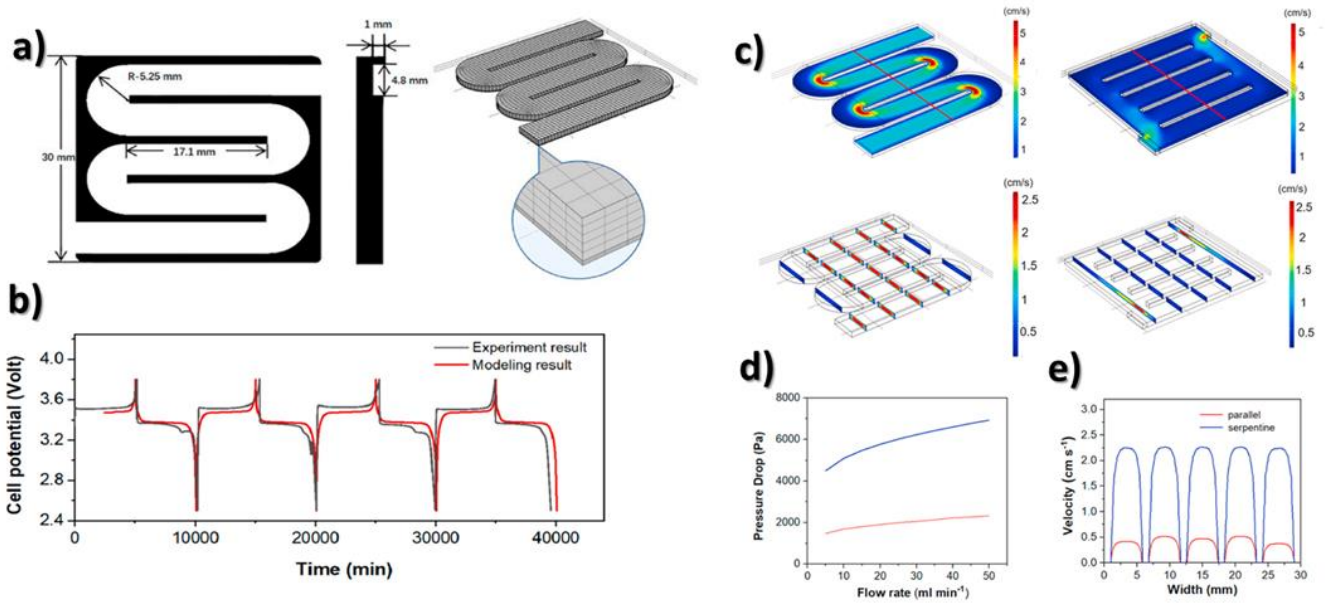

Fig. 8 (a) Detailed dimension of the flow field and computational meshes. (b) Comparison of the battery voltage between the model and experiment result. (c) Velocity distribution on the cross-sectional plane. (d) pressure drop as a function of the flow rate (e) velocity comparison on the middle cut line. Reproduced from ref. 159 with permission from Elsevier, Copyright 2022.

5. $LiFePO_4$ Based Redox Targeting Flow Lithium-ion Batteries

Although semi-solid technology is interesting, this approach presents apparent difficulties. For example, semi-solid slurries have low electronic conductivity and therefore an important quantity of conductive additives must be used to reduce the internal IR drop. In 2006, redox targeting of lithium-ion battery materials was proposed by Qizhao Huang and his colleagues to eliminate the need of expensive conductive additives, which offers a new concept for high-energy batteries. The lithiation/delithiation of the active material can be reversibly done by the diffusion of redox shuttle molecules in the electrolyte, assuring the transport of electrons between this active material in the tanks and the current collector in the electrochemical cell. In fact, this targeting process consists of two steps: the chemical delithiation/lithiation between the redox shuttle molecules and the active material, then the regeneration of the oxidized/reduced redox molecules at the electrode for another delithiation/lithiation. This concept can be applied for both cathodes and anodes and would lead to a novel energy storage device named redox targeting flow lithium-ion battery.[164]

5.1. 1,10-Dibromoferrocene ($FcBr_2$) and ferrocene (Fc) as LFP redox mediators

To demonstrate the concept of RFLB, Huang et al $LiFePO_4$ were successfully demonstrate a redox flow lithium-ion battery using $LiFePO_4$ as the active Li^+-storage material, and 1,10-Dibromoferrocene ($FcBr_2$) and ferrocene (Fc) as the redox mediators.[165] The redox targeting molecules used in this work were 1,10-Dibromoferrocene ($FcBr_2$) and ferrocene (Fc) presenting half-wave potentials (E1/2) of 3.55 and 3.25 V (vs. Li^+/Li), respectively, which make the reversible chemical delithiation/lithiation of $LiFePO_4$ (3.45 V) possible. During the charge, $FcBr_2$ oxidize at the electrode and $FcBr^{2+}$ species flow to the surface of $LiFePO_4$ and get reduced releasing lithium ion:

Reaction 1: $FcBr^{2+} + LiFePO_4 = FcBr_2 + FePO_4 + Li^+$

To complete the charge half cycle, $FcBr_2$ molecule move to the electrode and get oxidized. For the discharge half cycle, the injection of an electron into the $FePO_4$ is assured by using ferrocene molecule:

Reaction 2: $Fc + FePO_4 + Li^+ = Fc^+ + LiFePO_4$

FTIR and ex situ XRD analysis were carried out to investigate the chemical delithiation/lithiation processes and scrutinize the structural changes of $LiFePO_4/FePO_4$ caused by the redox mediators. The results have confirmed the reversible delithiation/lithiation of $LiFePO_4/FePO_4$ by $FcBr^{2+}$ and Fc. To investigate the feasibility of the concept, a RFLB half-cell was demonstrated. A reservoir containing 6.30 mg $LiFePO_4$ and 20 mM Fc and $FcBr_2$ dissolved in 1ml electrolyte solution was connected to the cathodic compartment. During

the first charging, the $LiFePO_4$ stored in the external reservoir was converted to $FePO_4$. Because of its higher E1/2, $FcBr_2$ could not reduce $FePO_4$, and this can be justified from the 2nd cycle in which only the capacity of $FcBr_2$ could be observed. Furthermore, much extended capacity was obtained by the addition of both redox mediators with $LiFePO_4$. The oxidation of Fc to Fc^+ and $FcBr_2$ to $FcBr^{2+}$ take place at the electrode with a slope from 3.40 to 3.50 V and 3.70 to 3.90 V, respectively, and the delithiation of $LiFePO_4$ by $FcBr^{2+}$ occurs in the reservoir (reaction 1), regenerating $FcBr_2$ with an extended plateau from 3.70 to 3.90 V. During the discharge, step c and d confirm the reduction of $FcBr^{2+}$ to $FcBr_2$ at 3.40 to 3.30 V, and then the reduction of Fc+ to Fc and the lithiation of $FePO_4$ by Fc shuttle molecule in the external reservoir (reaction 2). Moreover, the results prove that the lack of electric contact between the active material in the external reservoir and the electrode was related to the absence of both pairs of redox shuttle molecules, which explains the very low capacity of the cell.

The Li^+-conducting membrane is a further obstacle. The membrane must be both highly compact and have good Li^+ conductivity to avoid the crossover of redox shuttle molecules between the two electrode compartments. The current glass ceramic membrane exhibits high resistivity, poor chemical and mechanical stability, and short cycle life. These characteristics lead to significant overpotential loss. Recent developments in Li+-conducting polymeric membrane and lithium superionic conductors provide considerable promise for solving the problem.

5.2. I^-/I^{3-} and I^{3-}/I_2 as LFP redox mediators

Huang et al suggested a lithium-iodide redox flow lithium battery, which consists of a lithium anode and an iodide catholyte with $LiFePO_4$ as the energy storage material. This system can present high cycling stability and energy density due to the ability of $LiFePO_4$ to reach 22.8 M of Li^+ storage.[30] The iodide exhibits two redox reactions (I^-/I^{3-} and I^{3-}/I_2) in various solvents and show excellent chemical reversibility. In fact, as shown in the cyclic voltammetry (Fig. 9a), the I^-/I^{3-} reaction occurs at 3.15 V (vs. Li/Li^+) and the I^{3-}/I_2 reaction at 3.70 V (vs. Li/Li^+). Therefore, the redox potential of $LiFePO_4$ is at 3.45 V vs. Li/Li^+ (between the potentials of I^-/I^{3-} and I^{3-}/I_2). These results prove that $FePO_4$ can be chemically reduced by I^-, and $LiFePO_4$ can be chemically oxidized by I_2. Ex-situ X-ray diffraction (XRD) was carried out to study the structural changes of $LiFePO_4/FePO_4$ during the chemical delithiation/lithiation process (Fig. 9b). The delithiation and the lithiation of $LiFePO_4$ and $FePO_4$ occurs in the presence of 20 mM of I_2 and 20 mM of LiI, respectively. The delithiation of $LiFePO_4$ needs 20 minutes to be completed, while the lithiation of $FePO_4$ needs 2 hours as confirmed by the XRD patterns, which prove the reversible completion of the lithiation/ delithiation by I_2 and I^-, respectively. Fig. 9c shows that $LiFePO_4$ can be reversibly charged and discharged by I_2 and I^- in the catholyte. Moreover, low capacity was achieved in the absence of $LiFePO_4$. However, the addition of $LiFePO_4$ into the cathodic tank made the charging and discharging plateaus considerably longer. The RFLB cell also shows 90% capacity retention and 99% coulombic efficiency after 40 cycles (Fig. 9d).The gravimetric and volumetric energy densities of this system can reach ~370 Wh kg^{-1} and ~670 Wh L^{-1}, considering a $LiFePO_4$ porosity of 50% and a Li^+ storage concentration of 22.8 M. The performances are comparable to commercially available lithium-ion batteries[144] and vanadium redox flow batteries.[166] The studied system can achieve >10 times improvement in volumetric energy density by considering only the active material, this value can be higher if one considers the capacity brought by the redox species in the electrolyte.

The Li-I RFLB will become a significant high-density energy storage option for large-scale applications with further development of the flow design and Li^+-conductivity across the membrane.

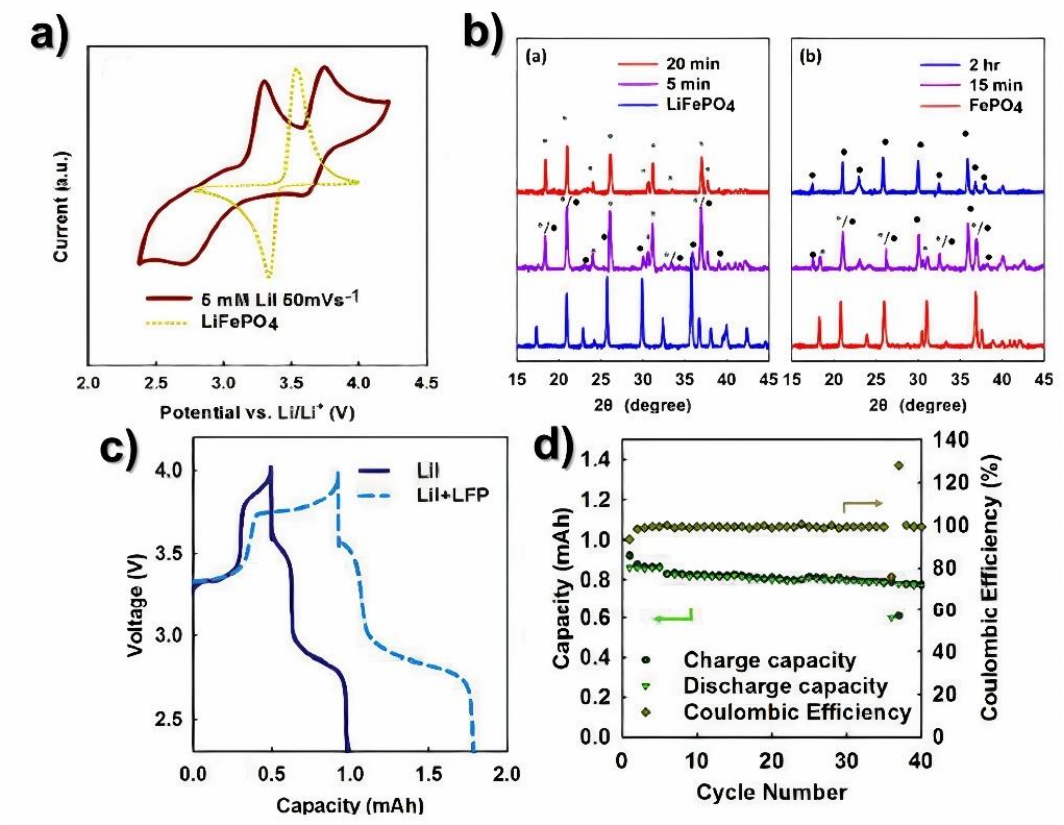

Fig. 9 (a) Cyclic Voltammograms of $LiFePO_4$ and the redox shuttle molecule LiI. (b) XRD patterns of LiFePO4/FePO4 during the chemical (a) delithiation and (b) lithiation. $FePO_4$ peaks are represented by * and $LiFePO_4$ peaks by ●. (c) Charge/discharge tests of the RFLB cell. (d) Capacity retention and Coulombic efficiency of the RFLB cell cycled at 0.075 mA cm^{-2} . Reproduced from ref. 28 with permission from Royal Society of Chemistry, Copyright 2016.

5.3. Dibromoferrocene ($FcBr_2$) and ferrocene (Fc) as LFP redox mediators

Jia et al have demonstrated a full cell redox flow battery by combining $LiFePO_4$ and TiO_2 as catholyte and anolyte respectively.[29] The problem encountered by the full cells is the need to use a mechanically and chemically stable membrane with low permeability of redox mediators and high conductivity of lithium ions. A polymeric Nafion/polyvinylidenedifluoride (PVDF) composite membrane was proposed in this work. Dibromoferrocene ($FcBr_2$), ferrocene (Fc), cobaltocene [$Co(Cp)_2$] and bis(pentamethylcyclopentadienyl)cobalt [$Co(Cp^*)_2$] were used in the catholyte and anolyte respectively as mediators for the redox targeting reactions, with $LiFePO_4$ and TiO_2 which are kept statically in two external reservoirs. The theoretical volumetric capacity of $LiFePO_4$ and TiO_2 can reach 613 and 603 Ah liter^{-1} due to their high Li^+ storage concentration of 22.8 and 22.5M (for $Li_{0.5}TiO_2$), respectively.[29] A full cell RFLB can reach an energy density higher than ~500 Wh l^{-1}, if considering a porosity of the materials in the reservoirs of 50%. This value is 10 times higher than the most developed vanadium RFBs. According to the Cyclic Voltammetry measurements, the potential of $LiFePO_4$ is 3.45 V (versus Li/Li^+), which is between the potentials of $FcBr_2$ (3.78 V) and Fc (3.40 V). Besides, on the anodic side, the potential of TiO_2 is 1.80 V and is between the potentials of $Co(Cp)_2$ (2.10 V) and $Co(Cp^*)_2$ (1.67 V). These results prove that $LiFePO_4$ and TiO_2 can be chemically reduced and oxidized by the studied redox mediators. Moreover, the cycling performances show the excellent stability of the capacity upon cycling. The obtained results have demonstrated the feasibility of full cell RFB using Nafion/PVDF composite membrane. In fact, an energy density five times higher than that of VRB was achieved. In addition, the cell showed a good cycling due to the low crossover of the redox molecules. However, the conductivity of the Li^+-conducting Nafion/PVDF membrane needs to be further improved for use in real applications. Additionally, the redox molecules employed here are far from perfect, and as a result, their reactions with $LiFePO_4$ and TiO_2 result in intolerably high overpotential losses. It is envisaged that the full development of RFLB would offer a game-changing approach to obtaining high-energy density large-scale electrochemical storage with a good Li+-conducting membrane and adequate redox mediators.

5.4. 2,3,5,6 tetramethyl-p-phenylenediamine (TMPD) as bi-functional LFP redox mediator

A bi-functional redox mediator 2,3,5,6 tetramethyl-p-phenylenediamine (TMPD) with improved cycling life and voltage efficiency was proposed by Guang Zhu et al.[31] The cyclic voltammogram of this mediator show two pairs of peaks at 3.20 and 3.60 V vs. Li/Li^+ as presented in Fig. 10a (the reaction of $TMPD/TMPD^{\bullet+}$ and $TMPD^{\bullet+}/TMPD^{\bullet 2+}$, respectively).

- **During the charging process, the reactions taking place are:**

$$TMPD^{\bullet+} - e^- = TMPD^{\bullet 2+} \text{ (on electrode)}$$

$$TMPD^{\bullet 2+} + LiFePO_4 = TMPD^{\bullet+} + Li^+ + FePO_4 \text{ (in tank)}$$

- **During the discharging process the reactions taking place are:**

$$TMPD^{\bullet+} + e^- = TMPD \text{ (on electrode)}$$

$$TMPD + Li^+ + FePO_4 = TMPD^{\bullet+} + LiFePO_4 \text{ (in tank)}$$

Fig. 10b show the existence of two voltage plateaus corresponding to the two oxidation potentials of TMPD. The coexistence of TMPD and $LiFePO_4$ in the catholyte extend the discharge time ~7 times than that containing only TMPD. Additionally, as shown in Fig. 10c, the XRD patterns show that the $LiFePO_4$ granules were converted to $FePO_4$ during the charging, which are then reversed back to $LiFePO_4$ during the discharge. Due to its ability to identify the valance states, coordination environment and geometric distortions of elements in battery materials, [167,168] the XANES Operand technique has been employed to reveal the evolution of $LiFePO_4$ in the reservoir during charging and discharging. Fig. 10d, e show the absence of absorption at the first charging plateau, which signifies that the process involves only the oxidation of TMPD to $TMPD^{\bullet+}$ without any oxidation of $LiFePO_4$. However, the absorption edge of Fe shifted towards higher energy at the second plateau, indicating that the oxidation of $LiFePO_4$ to $FePO_4$ by the redox mediator occurs at the second charging plateau.

Despite the encouraging results, future research must concentrate on improving the stability of TMPD-based electrolyte in order to create a reliable RFLB system.

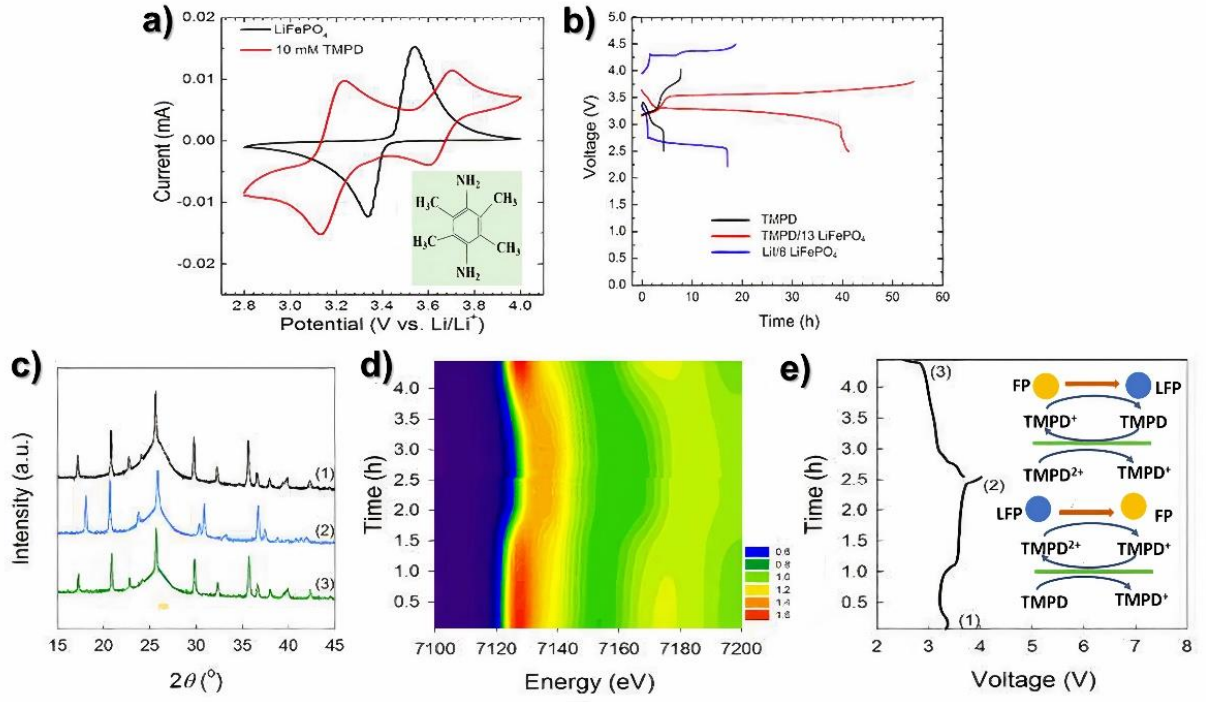

Fig. 10 (a) Cyclic Voltammograms of 10 mM $TMPD^{\bullet+}$ (red curve) and $LiFePO_4$ (black curve) in 0.5 M LiTFSI/DEGDME electrolyte at a scan rate of 50 mV/s. The inset present the molecular structure of TMPD. (b) Charge/discharge profiles of the RFLB cell. (c) XRD patterns of $LiFePO_4$ at different stages of charge/discharge

(refer to *e*). (d) Evolution of the near edge energy of Fe in $LiFePO_4/FePO_4$ at different time of charge/discharge. (e) Voltage profile of the RFLB subjected for XANES measurement. The inset illustrates the redox targeting reactions. Reproduced from ref. 29 with permission from American Chemical Society, Copyright 2017.

5.5. $[Fe(CN)_6]^{4-}/[Fe(CN)_6]^{3-}$ as LFP redox mediator

In another study, $[Fe(CN)_6]^{4-}/[Fe(CN)_6]^{3-}$ and S^{2-}/S_2^{2-} were used as redox mediators for $LiFePO_4$ and $LiTi_2(PO_4)$ in catholyte and anolyte, respectively (Fig. 11a). This aqueous system reported by Yu et al could deliver a volumetric capacity of 603 and 308 Ah L^{-1} for a lithium concentration in $LiFePO_4$ and $LiTi_2(PO_4)_3$ of 22.5 and 11.5 M respectively, higher than all VRFBs reported in the literature.[145] In 0.1 M LiOH electrolyte, the redox potential of $LiFePO_4$ is 0.21 V (vs.Hg/HgO), and that of $LiTi_2(PO_4)_3$ is -0.69 V (vs. Hg/HgO). Besides, the widely studied $[Fe(CN)_6]^{4-}/[Fe(CN)_6]^{3-}$ has a redox potential of 100 mV, more positive than that of $LiFePO_4$, and has excellent reversibility and solubility in water.[148] Moreover, the polysulfides, already used as anolyte for various redox flow batteries[169–171] have a redox potential comparable to that of $LiTi_2(PO_4)_2$ (0.69 V (vs. Hg/HgO)). These cyclic voltammetry results prove that the studied redox mediators can reversibly oxidize and reduce the active materials (Fig. 11b, c).

- The electrochemical reactions at the electrodes are:

$$[Fe(CN)_6]^{4-} = [Fe(CN)_6]^{3-} + e^-$$

$$S_2^{2-} + 2e^- = 2S^{2-}$$

- The chemical reactions in the reservoirs are:

$$[Fe(CN)_6]^{3-} + LiFePO_4 = [Fe(CN)_6]^{4-} + FePO_4 + Li^+$$

$$2S^{2-} + LiTi(PO_4)_3 + 2Li^+ = S_2^{2-} + Li_3Ti_2(PO_4)_3$$

X-ray photoelectron spectroscopy (XPS) (Fig. 11d) was carried out to investigate the reaction between $LiTi_2(PO_4)_3$ and S^{2-}/S_2^{2-}. After immersing in 1 M Li_2S solution for 12 hours, the valence state of Ti in $LiTi_2(PO_4)_3$ changed from Ti^{4+} to Ti^{3+}, suggesting that $LiTi_2(PO_4)_3$ has been reduced by S^{2-} to form $Li_3Ti_2(PO_4)_3$, which then oxidized by S_2^{2-} after immersing in Li_2S_2 solution). As shown in Fig. 11e, the system presented a discharge voltage of 0.7 V at a current density of 5 mA cm^{-2}. The cathodic compartment delivered a charge capacity of 152 mAh with an utilization ratio of 43.7 % using 0.90g of $LiFePO_4$. This charging capacity increased to 420 mAh when using 2.69 g of $LiFePO_4$ with higher porosity (utilization of 73.3%). The studied cell exhibited also high-capacity retention of 99.1% after 55 cycles, and good cycling stability at a current density of 5 mA cm^{-2}, as shown in Fig. 11f. Besides, the power density was 8 mW cm^{-2} at 100% SOC, with a current density of 20 mA cm^{-2}.

In conclusion, the proposed system reveals enhanced electrochemical performances, it delivered improved energy density and a volumetric capacity for the cathodic and anodic reservoirs of 76 and 141 Ah L^{-1}, respectively. These results can be further enhanced to 305 and 207 Ah L^{-1} by a simple optimization of the loading and the utilization ratio of the static active materials in the reservoirs. Moreover, the power density can be improved by using a better anodic electrocatalyst for polysulfide.

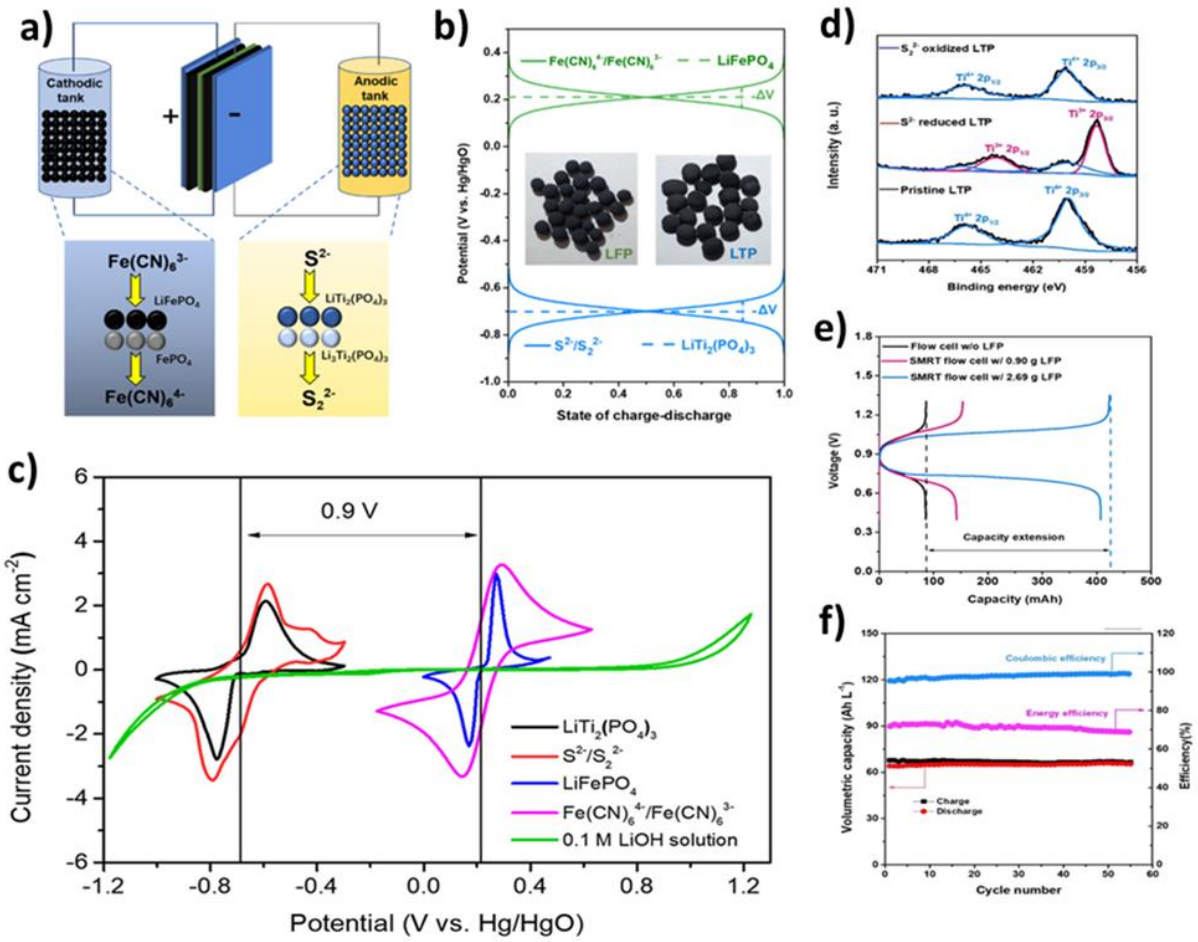

Fig. 11 (c) Cyclic voltammograms of $LiFePO_4$ and $LiTi_2(PO_4)_3$ as well as the redox mediators. (d) XPS spectra of Ti2p in $LiTi_2(PO_4)_3$ after lithiation by S^{2-} and delithiation by S_2^{2-}. (e) Charge/ discharge profiles of a full cell. (f) Cycling performance of a full cell with 0.90 g $LiFePO_4$ and 1.0 g $LiTi_2(PO_4)_3$ granules in 7 mL (0.3 M) $K_4Fe(CN)_6$ catholyte and 4 mL (1 M) Li_2S_2 anolyte. Reproduced from ref. 141 with permission from American Chemical Society, Copyright 2018.

5.6. Ferri/Ferrocyanide complexes as redox mediator for Porous $LiFePO_4$ pellets

Vivo-Vilches et al. have suggested an optimized new catholyte using porous $LiFePO_4$ pellets as lithium storage material, ferri/ferrocyanide complexes as redox mediator and DMSO/water mixture as electrolyte.[172] The prepared $LiFePO_4$ particles coated with 1.8 % carbon were then mixed with NaCl using two different LFP/NaCl volume ratios (70/30 and 60/40), and the LFP pellets will be named as LFP30 and LFP40, respectively. Fig. 12a shows the evolution of Cyclic Voltammetry signal of $[Fe(CN)_6]^{4-}$ solutions in a mixture of DMSO and water. It is clearly observed that when the vol % of DMSO increases, the Cyclic Voltammetry curve shifts towards lower voltage. Moreover, the redox potential of $FePO_4/LiFePO_4$ in the working conditions is E = 0.37 V vs. SHE, indicating that a mixture of solvent composed of 20 vol% of DMSO and 80 vol% of H_2O is the most appropriate solvent to have a good match between the potential of $LiFePO_4$ and that of the mediator. X-ray diffraction (XRD) was performed to study the structural changes of $LiFePO_4/FePO_4$ during the chemical delithiation/lithiation by the redox mediators (Fig. 12b). The XRD patterns are unchanged when a solution with low content of $[Fe(CN)_6]^{3-}$ is used (0, 25 or 50 %). However, the $FePO_4$ diffraction peaks appear clearly when using 100% of $[Fe(CN)_6]^{3-}$, indicating the oxidation of $LiFePO_4$ into $FePO_4$. For the reduction process, $FePO_4$ reverts to $LiFePO_4$ when using 100% $[Fe(CN)_6]^{4-}$ solution. The galvanostatic test of the electrolyte alone (0.2 M $Fe(CN)_6^{4-}$ in DMSO/H_2O (20/80 vol/vol) + LiCl 0.5 M) (Fig. 12d, black curve) reveals its full reversibility and good capacity. After adding 1.85 g of LFP30 pellets, the capacity was increased by 170 mAh for the charge (Fig. 12d, green curve), signifying a utilization ratio of 54% of LFP. This result is the same obtained by Yu et al[145] for $LiFePO_4$ with another solvent mixture. In other words, the addition of 1% vol. of LFP increases the total capacity by 30 % at a current density of 1 mA cm^{-2}, and up to 50 % at a current density of 0.25 mA cm^{-2}.

As a conclusion, a system with high columbic efficiency and huge capacity was developed. This work may serve as a proof-of-concept for the effect of material processing and cell design on the performance of RT-RFBs, but the scope may be expanded to include larger scale optimizations and a wider range of mediator/insertion material pairs.

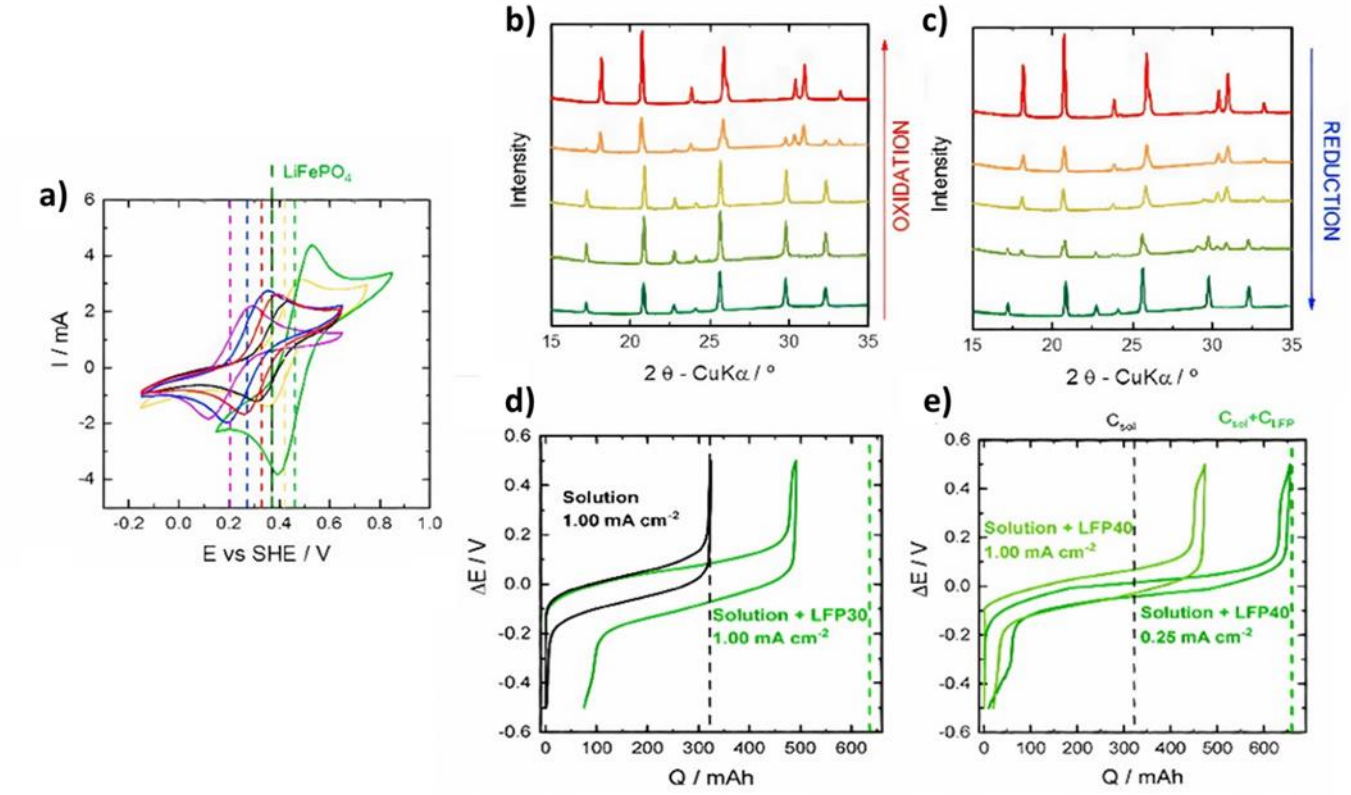

Fig. 12 (a) Cyclic voltammograms of $K_4Fe(CN)_6$ solutions in different DMSO/H_2O mixtures with LiCl 0.5 M as supporting electrolyte. (b) XRD patterns of $LiFePO_4$ in solutions with increasing concentrations of $[Fe(CN)_6]^{3-}$, and (c) in solutions with increasing concentrations of $[Fe(CN)_6]^{4-}$. (d) Charge/discharge tests for RFB containing 60 mL of 0.2 M $K_4Fe(CN)_6$ as catholyte and 180 mL of 0.2 M $K_3Fe(CN)_6$ as anolyte. (e) Battery containing 60 mL of 0.2 M $K_4Fe(CN)_6$ as catholyte and 180 mL of 0.2 M $K_3Fe(CN)_6$ as anolyte. Reproduced from ref. 168 with permission from Elsevier, Copyright 2021.

5.7. FcIL ionic liquid as LFP redox mediator

The Nernstian-potential-driven redox-targeting reaction refers to a specific approach that can improve the performance of $LiFePO_4$-based redox flow batteries. In this context, Mingyue Zhou et al. proposed a single-molecule redox-targeting (SMRT) concept using ionic liquid grafted with ferrocene, that has a standard potential that matches that of $LiFePO_4$.[173] Fig. 13 depicts a schematic illustration of the RFLB half-cell used in this study, with an energy storage tank containing granules of $LiFePO_4$ (Fig. 13b). The chosen redox mediator, FcIL (Fig. 13c), is an ionic liquid with a ferrocene group attached to a methylimidazolium ion. This compound has been carefully selected due to its suitability for the intended purpose. Cyclic voltammetry

analysis reveals that its half-wave potential is approximately 3.43 V (relative to Li/Li$^+$). This value closely matches that of $LiFePO_4$ in an electrolyte consisting of 1 M lithium bis(trifluoromethanesulfonyl)amide (LiTFSI) dissolved in propylene carbonate (PC) (Fig. 13d). Therefore, FcIL is an ideal candidate to be used in this system.

Both static and flow cells were utilized to investigate the SMRT reactions in battery applications. Results from Fig. 13e indicate that upon introducing 0.44 M equivalent $LiFePO_4$ granules into the cathodic compartment, the static cell demonstrated a prolonged voltage plateau beyond the capacity of 0.50 M FcIL present in the catholyte. This utilization of SMRT reactions accounted for over 50% of the material's usage, whereas the $LiFePO_4$ powder itself showed minimal capacity in the absence of FcIL. The cell showed only one voltage plateau, effectively reducing voltage loss and significantly improving voltage efficiency to approximately 95%. After five cycles, the cell retained about 90% capacity, indicating satisfactory stability of the system. It was observed that some electrolyte was trapped at the gasket gap after testing, which could be responsible for the capacity drop observed during testing.

To provide further evidence for the viability of using the SMRT reaction, a flow cell was utilized. The results displayed in Fig. 13f reveals that upon adding 0.37 M (13.1 mAh) equivalent $LiFePO_4$ granules to the tank, the voltage plateau of 0.20 M FcIL was significantly prolonged. This prolonged voltage plateau exceeded the discharge capacity of the molecule by 2.1 times. When utilizing flow through mode, the chemical reactions between the redox molecules and solid material were notably enhanced due to the forced mass transport. As a result, the utilization of $LiFePO_4$ was improved up to 95%.

In summary, the SMRT reaction offers an elegant way to enhance voltage efficiency while preserving the key features of redox-targeting-based RFBs. This approach simplifies the electrolyte composition of the cell. During charge-discharge cycles, small potential differences originating from activity changes of redox-active species enable reversible delithiation and lithiation of $LiFePO_4$. A single molecule can achieve near-unity utilization yield and 95% voltage efficiency, leading to a significant increase in volumetric tank energy density to 330 Wh L^{-1}, which can be optimized up to 942 Wh L^{-1}. To achieve balanced power generation and energy storage for practical applications, researchers will extensively explore robust redox mediators with superior kinetics and solid material granules with optimized quantity and packing density.

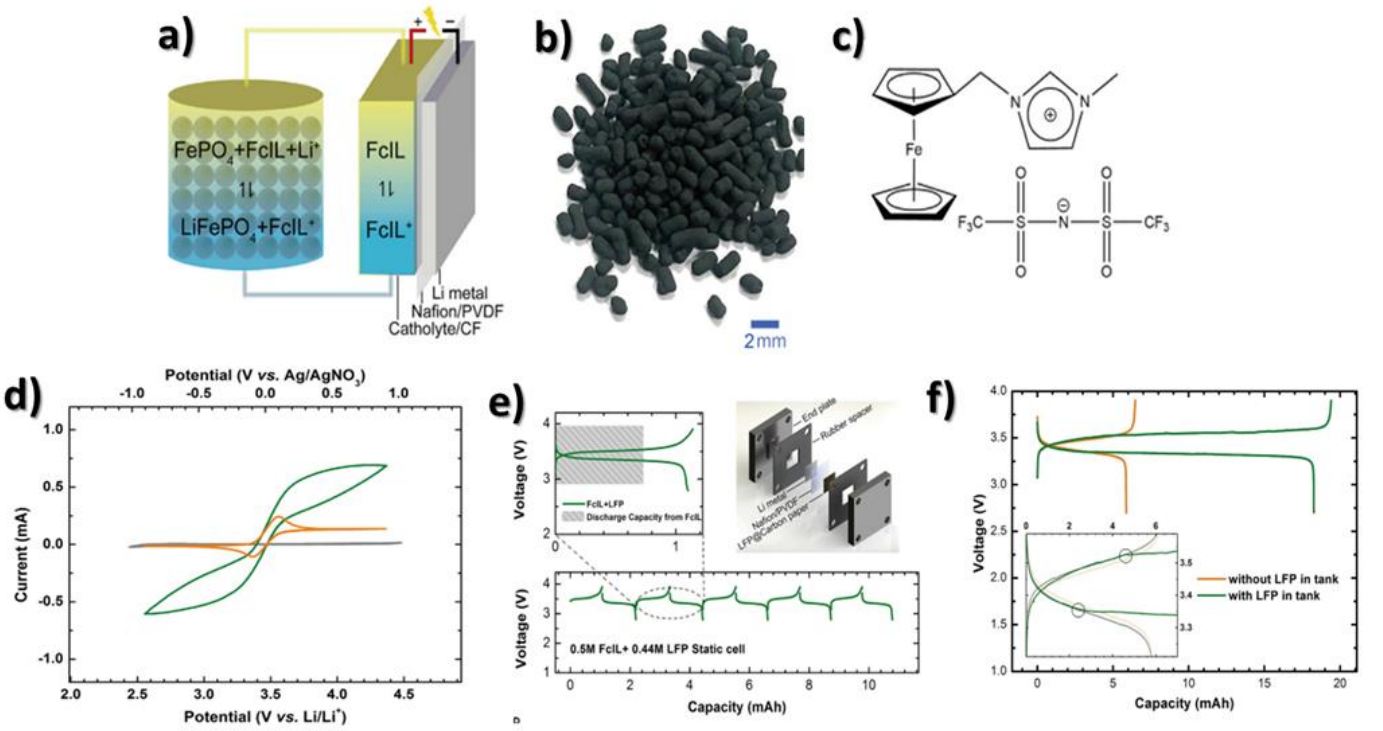

Fig. 13 (a) Schematic of an RFLB half-cell with $LiFePO_4$ granules filled in the energy storage tank. (b) The $LiFePO_4$ granules. (c) Molecular structure of FcIL. (d) Cyclic voltammograms of 50 mM FcIL on a double-layer electrode in the absence (orange) and presence (green) of $FePO_4$/$LiFePO_4$ (1:1). For comparison, the gray curve shows the CV of a $FePO_4$/$LiFePO_4$-coated double-layer electrode in the absence of FcIL in the electrolyte. The electrolyte was 1 M LiTFSI/PC. The scan rate was 2 mV/s. (e) galvanostatic voltage profile, exploded view of the static cell, and voltage profiles of the static cell for five consecutive cycles. (f) Voltage profiles of flow cells with 0.20 M FcIL in the catholyte and 0.37 M equivalent $LiFePO_4$ granules in the tank. Reproduced from ref. 169 with permission from Elsevier, Copyright 2017.

5.8. $[Fe(CN)_6]^{3-}$ as LFP redox mediator with Packed bed flow reactor

To study the kinetics of the electrochemical reactions in the electroactive material and the effects of different parameters, such as temperature, pressure, and electrolyte composition, on the electrochemical behavior of the RTFBs. Devanshi Gupta et al. developed a packed bed flow reactor (PBR) that allows the precise control of the flow rate and concentration of the electrolyte solution.[174] The studied redox targeting system comprises interlinked electrochemical and chemical reactors, as depicted in Fig. 14a. The system involves a power stack in which redox shuttles are subjected to electrochemical oxidation or reduction, and storage tanks that contain solid electroactive materials, which undergo chemical redox reactions with the redox shuttles. Fig. 14b shows a three-dimensional reconstruction of the packed bed of $LiFePO_4$ (as used in the experimental setup) from X-ray computed tomography which can provides valuable insights into the microstructure and performance of the packed bed.

The effect of the Bed-height was carefully studied. In fact, the height of the PBR was altered at 0.5, 1.0, and 1.5 cm while keeping the mass of LFP powder per bed volume and flow-rate constant. For all experiments conditions, the concentration of $[Fe(CN)_6]^{3-}$ was 0.2 mol L^{-1}, and the flow rate

was of 30 mL hr^{-1} at room temperature. The time during which the feed solution passed through the PBR was selected to ensure that the volume of electrolyte flowing through each bed height contained twice the number of moles of the redox shuttle compared to the moles of LFP present in the packed bed reactor. The conversion of LFP solid material in the reactor as a function of effluent volume/reaction time (Fig. 14c, d) showed much more variation for the two shorter bed heights (0.5 and 1.0 cm). This can be explained by the creation of areas within the bed where the fluid bypasses some of the particles, causing those regions or particles to not react completely. This could lead to a higher degree of variation in LFP conversion for columns with smaller total thickness or volume, as any bypassed zones would have a larger impact on the overall measured conversion of LFP in the column. When two moles of $[Fe(CN)_6]^{3-}$ per mole of LFP were flowed through packed beds of varying heights, the molar conversion of LFP to FP ranged from 81% to 88%, with slightly higher conversion observed at a bed height of 1.5 cm. However, when equivalent molar stoichiometries of $[Fe(CN)_6]^{3-}$ were flowed through beds of different heights, the molar conversion of LFP was similar, indicating that proportional total moles of $[Fe(CN)_6]^{3-}$ solution played a key role in the conversion of LFP. When the same amount of $[Fe(CN)_6]^{3-}$ solution (30 mL, 6 mol) was flowed through different bed heights, a significant difference in the molar conversion of LFP was observed. Thus, for the same moles of redox shuttle flowed through, the molar conversion of LFP was dependent on bed height, as shown in Fig. 14e. However, for the same molar ratio of LFP to redox shuttle, there was no significant difference in conversion.

The effect of Flow rate variation, Redox shuttle concentration, and temperature were also examined. The molar conversion of the LFP packed bed was found to be unaffected by changing the flow rate of the $[Fe(CN)_6]^{3-}$ solution within the range of 30 to 66 mL hr^{-1}. Therefore, the variation in flow rate did not result in any significant effect on the molar conversion of the LFP packed bed. Besides, Devanshi Gupta et al. evaluated three different concentrations of $[Fe(CN)_6]^{3-}$ solution (0.1, 0.2, and 0.3 mol L^{-1}) at room temperature, using a constant flow rate of 54 mL h^{-1}, with a bed height of 1.0 cm and 1.0 g LFP. As illustrated in Fig. 14f, the concentration of the redox shuttle had an impact on the molar conversion of LFP in the packed bed reactor. The LFP was converted to FP more rapidly as the concentration of $[Fe(CN)_6]^{3-}$ increased. When 60 mL of 0.3 mol L^{-1} $[Fe(CN)_6]^{3-}$ solution passed through the reactor, the LFP was fully delithiated. However, when the same volume of 0.1 mol L^{-1} $[Fe(CN)_6]^{3-}$ solution was used, only 56% conversion of LFP to FP was achieved. Finally, to study the effect of temperature variation, a water bath was used to keep the PBR at constant temperature. The conversion of LFP in the PBR was 53.5% and 75% after 60 mL of feed solution had exited the reactor at 4.0 and 13.0 °C, respectively. At higher temperatures of 22.4 and 40.0 °C, both conversions were similar at 80%. The four temperature variations resulted in significant differences in conversion, with the conversion at 4 °C being much lower than at higher temperatures. The PBR may have limiting processes at the primary particle level (such as electron transfer kinetics and Li^+ diffusion) at temperatures below 20 °C, which could explain the lower conversion at 4 °C. In addition, the transport of $[Fe(CN)_6]^{3-}$ in the liquid phase would be slowed at lower temperatures due to the dependence of its diffusion coefficient.

In summary, the study presents a model for examining the behavior of Li-ion electroactive materials in packed beds as they undergo chemical redox. This is significant for redox targeting flow battery applications and has potential implications for processes such as the recovery and extraction of Li^+ from used Li-ion battery materials. However, more understanding of the fundamental principles of the reaction and the factors that influence its performance are required to optimize the system design and potentially develop new and improved materials for use in these applications.

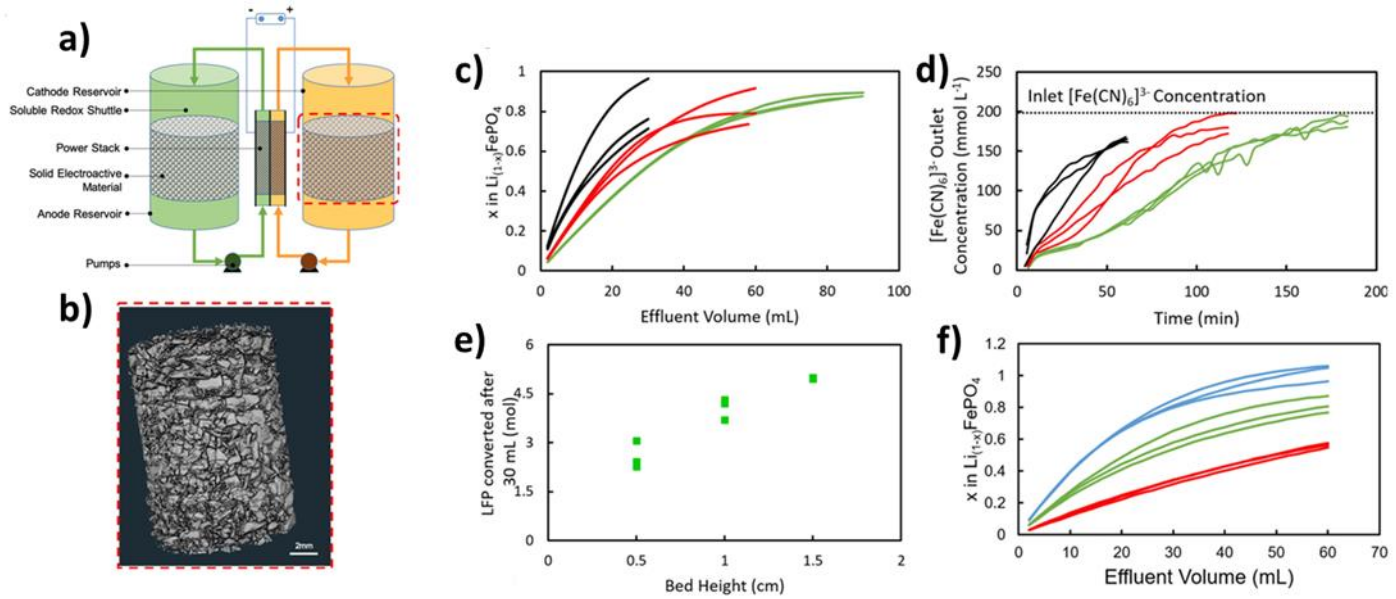

Fig. 14 (a) Schematic illustration of a full cell redox targeting flow battery. (b) Three-dimensional reconstruction of a packed bed of $LiFePO_4$ as used in the experimental setup. (c) The conversion of LFP solid material in the reactor as a function of the effluent volume of redox shuttle solution fed, at bed heights of 0.5 cm (black), 1.0 cm (red), and 1.5 cm (green). d) The outlet concentration of $[Fe(CN)_6]^{3-}$ as a function of time. e) The total moles of LFP converted (FP generated) as a function of bed height, with a constant 30 mL volume of 0.2 mol L^{-1} $[Fe(CN)_6]^{3-}$ flowed through the column. (f) Conversion of LFP to FP with a concentration of redox shuttle of 0.1 mol L^{-1} (red), 0.2 mol L^{-1} (green), and 0.3 mol L^{-1} (blue) as a function of the volume of feed solution. Reproduced from ref. 170 with permission from Elsevier, Copyright 2022.

5.9. Tetrathiafulvalene (TTF) as LFP redox mediator

To be practical for commercial and industrial applications, RFBs must have certain performance characteristics, including high energy density, long cycle life, and low cost. One promising approach is to use organic bifunctional redox mediators (BRMs) to enhance the electrochemical performance of the battery.[175] BRMs can shuttle electrons between the positive and negative electrolytes, increasing the effective concentration of the redox-active species and improving the cell voltage. In this context, a research group from the University of Science and Technology of China recently developed a high

energy density 3V-class redox flow battery using $LiFePO_4$ and graphite with organic BRMs. The battery consists of solid active materials $LiFePO_4$ and graphite in the cathodic and anodic tank, respectively, and the bifunctional mediators were circulated between the tanks and the electrochemical cell to ensure the oxidation/reduction reaction of the static active materials. The researchers used two different BRMs: tetrathiafulvalene (TTF) with $LiFePO_4$ for the positive side, and graphite with biphenyl for the negative side. The Cyclic Voltammetry of TTF mediator showed two reversible redox reactions at 3.31 V and 3.58 V vs. (Li/Li^+) which correspond to the reactions described in following equations:

$$\textbf{(1) TTF} \rightarrow \textbf{TTF}^{+} + e^{-} \qquad \textbf{3.31V vs. (Li/Li}^{+}\textbf{)}$$

$$\textbf{(2) TTF} + \rightarrow \textbf{TTF}^{2+} + e^{-} \qquad \textbf{3.58V vs. (Li/Li}^{+}\textbf{)}$$

The redox potential of $LiFePO_4$ (3.5V) is situated between the first and second redox potentials described in Eq. (1) and Eq. (2) respectively. This indicates that the redox potentials of TTF can be utilized to charge and discharge the battery. A half-cell charge-discharge test was conducted using electrochemically charged/discharged TTF to confirm the charge/discharge of $LiFePO_4$. The test results for the positive-side half-cell are illustrated in Fig. 15a. The addition of $LiFePO_4$ to the positive electrode side increased the charge capacity by 19.8 µAh, which is equivalent to 28.4% of the added $LiFePO_4$ compared to the case without active material. This indicates that the system with active material has an increased charge and discharge capacity when compared to the system without active material. The results suggest that TTF oxidizes and reduces $LiFePO_4$. Furthermore, the reversibility of biphenyl's redox reaction was studied using Cyclic Voltammetry measurements. The result shows the existence of a single reversible redox pair, which exhibited an oxidation potential of 0.42 V and a reduction potential of -0.02 V vs. (Li/Li^+). LiC_6 has a redox potential of 0.01 V vs. (Li/Li^+), which exceeds the reduction potential of biphenyl. This indicates that charged biphenyl has the capability to reduce the graphite. Moreover, to verify the discharge process of LiC_6 by biphenyl as a mediator, a discharge verification test was performed. The discharge voltage profile, as depicted in Fig. 15b, illustrates an increase in the discharge capacity upon the inclusion of LiC_6 in the cell. This enhanced capacity is believed to be a result of the involvement of LiC_6.

Finally, the researcher conducted a proof-of-concept test on the flow-type cell by combining the positive and negative electrode systems described earlier. Fig. 15c displays the charge-discharge voltage profile using a full cell. Without the active material, the positive electrolyte would have a designed capacity of 0.7 mAh since 3 mL positive electrolyte comprises 5 mM TTF. However, the charge-discharge voltage curve indicates that the capacity exceeded the theoretical capacity in the absence of the active material. This implies that the additional capacity was extracted from the added active materials. The mediator molecules are oxidized/reduced at the electrode, and subsequently, the mediators chemically oxidize/reduce the active material.

Overall, these results demonstrate the potential of organic BRMs for enhancing the electrochemical performance of RFBs and suggest that $LiFePO_4$/graphite RFBs with organic BRMs could be a promising technology. However, the coulombic efficiency of the system is currently at 83.2%, which is low since only 31% of the theoretical capacity of $LiFePO_4$ is being utilized. This implies that there is a significant amount of uncharged $LiFePO_4$ remaining in the tank, which reacts chemically with charged TTF, resulting in a decreased discharge capacity. To improve the coulombic efficiency and utilization of active materials, increasing the concentration of the redox mediator in the solution is an effective way to accelerate the chemical reaction between the mediator and the active material.

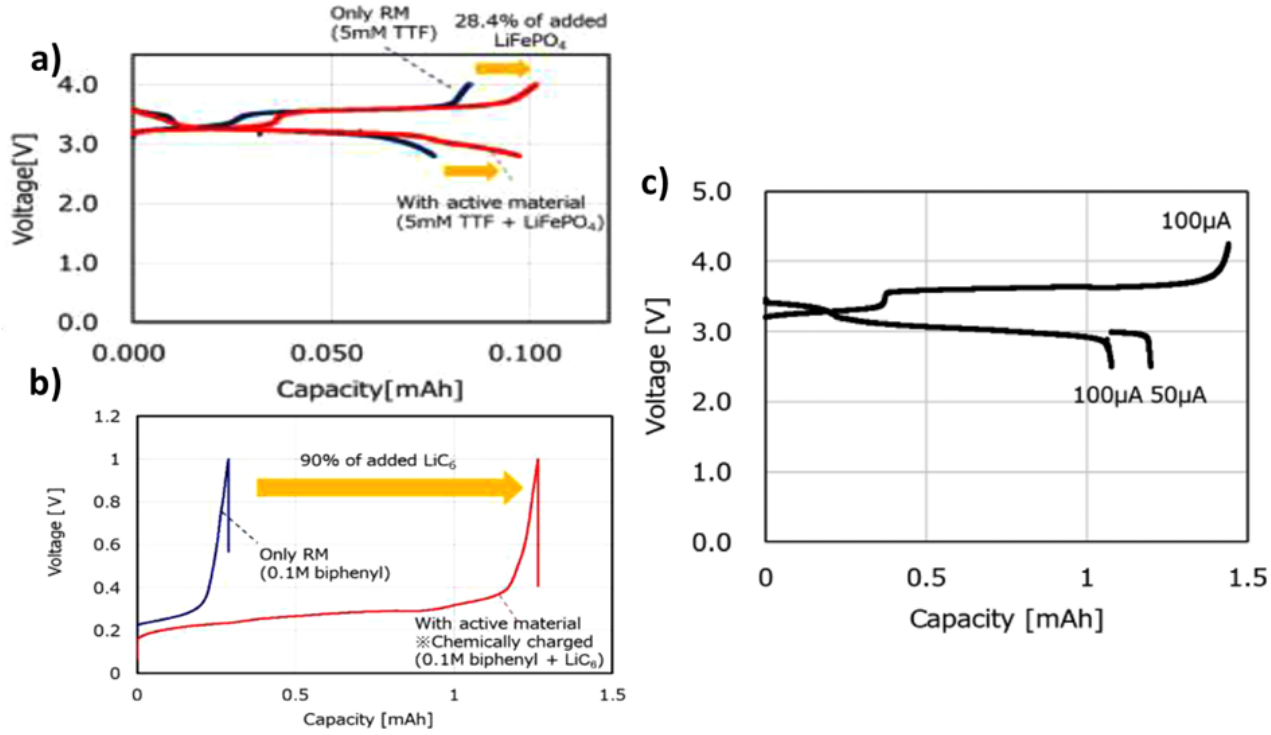

Fig. 15 (a) Electrochemical performance of the negative-electrode side half-cell. (b) Electrochemical performance of the positive-electrode side half-cell. (c) Electrochemical performance of the redox-flow type full-cell. Reproduced from ref. 171 with permission from Elsevier, Copyright 2022.

Table 2 Summary of the different works using $LiFePO_4$ as active material for Semi-Solid and Targeting redox flow batteries.

Cathode material	wt% conductive additive	wt% material	Anode material	Electrolyte	LFP particle size	Volumetric Energy
$LiFePO_4$	Without conductive additive	40 vol% $LiFePO_4$	Lithium metal	M $LiPF_6$ in EC/DEC	0.210 and 18 µm (commercial)	~230 Wh L^{-1}
$LiFePO_4$	1.5 wt % Ketjenblack	22 wt % $LiFePO_4$	Zinc metal	1 M $ZnSO_4$/0.2 M Li_2SO_4	0.210 and 18 µm (commercial)	~50 WhL^{-1}
$LiFePO_4$	23 wt% Ketjen Black	77 wt% $LiFePO_4$	$LiTi_2(PO_4)_3$	21 m LiTFSI and 1 m ZnTFSI	0.210 and 18 µm (commercial)	74 Wh L^{-1}
$LiFePO_4$/ 15 CNTs	0.1 wt % Ketjenblack	0.9 wt % $LiFePO_4$/15CNTs	Lithium metal	1 M $LiPF_6$ dissolved in EC:EMC:DMC = 1:1:1	0.5–1 µm	~50 Wh L^{-1}
Cathode material	**Mediators**	**[Mediators]**	**Anode material**	**Electrolyte**	**LFP loading mass**	**Volumetric Energy**
$LiFePO_4$	$FcBr_2$ and Fc	20 mM	$Li_4Ti_5O_{12}$	1 M $LiPF_6$ in DMC	6.30 mg	~200 WhL^{-1}
$LiFePO_4$	I^-/I_3^- and I_3^-/I_2	20 mM of I_2 and 20 mM of LiI	Lithium metal	1 M LiTFSI/TEGDME	6.4 mg	~670 Wh L^{-1}
$LiFePO_4$	$FcBr_2$, Fc, $[Co(Cp)_2]$ $[Co(Cp^*)_2]$	5 mM $Co(Cp)_2$/$Co(Cp^*)_2$ and 5 mM $FcBr_2$/Fc	TiO_2	1 M $LiPF_6$ in DMC	6.4 mg	~500 Wh L^{-1}
$LiFePO_4$	TMPD	25 mM	Lithium	1 M LiTFSI/TEGDME	158 mg	1023 WhL^{-1}
$LiFePO_4$	$[Fe(CN)_6]^{4-}/[Fe(CN)_6]^{3-}$ and S^{2-}/S_2^{2-}	0.3 M $K_4Fe(CN)_6$	$LiTi_2(PO_4)_3$	1 M $LiNO_3$, and 0.1 M LiOH + 30 vol % TEGDME	2.69 g	~76 and 141 Ah L^{-1}
$LiFePO_4$	ferri/ferrocyanide	0.1 M $[Fe(CN)_6]^{3-}$	0.2 M $K_3Fe(CN)_6$	0.5 M LiCl in DMSO/water	2 g	600 Ah L^{-1}
$LiFePO_4$	Tetrathiafulvalene (TTF) and biphenyl	5 mM TTF 0.1 M Biphenyl	Graphite	Cathode: 1M $LiBF_4$ in PC Anode: $LiBF_6$ in 2-MeTHF	0.416 g	-
$LiFePO_4$	Ferrocene-grafted ionic liquid (FcIL)	0.2 M FcIL	Lithium	1 M LiTFSI/PC	18.5 g	330 Wh L^{-1}

ARTICLE

Table 3 Comparison between the different Varieties of RFBs

			Negative electrolyte	Positive electrolyte	OCV (V)	Volumetric enegy (Wh/L)	Ref
All-liquid RFBs	Inorganic Solutes	All- Vanadium	V(II)/V(III)	V(IV)/V(V)	1.26	25 -42	176
		Vanadium-Bromine	V(II)/V(III)	Br_2/Br^-	1.3	35-70	177
		Vanadium-Chromium	Cr(III)/Cr(II)	V(II)/V(III)	1.59	37.79	178
		polysulfide/iodide	S^{2-}/S_2^{2-}	I^-/I^{3-}	1.05	43.1	170
		Iron-Chromium	Cr(II)/Cr(III)	Fe(II)/Fe(III)	1.18	15.8	176
	Organic Solutes	Quinone-Bromide	Quinone/ HydroQuinone	Br_2/Br^-	0.92	-	179
		Anthraquinone-Benzoquinone	AQS/H_2AQS	BQDS/H_2BQDS	1.0	-	180
		Symmetric $[(bpy\text{-}(CH_2)_3NMe_3)]I_2$	$[(bpy\text{-}(CH_2)_3NMe_3)]I_2$	$[(bpy\text{-}(CH_2)_3NMe_3)]I_2$	1.38	32.5	181
Hybrid RFBs		Zinc-Cerium	Zn	Ce(III)/Ce(IV)	2.5	20-37	182
		Zinc/4,4′,4″-trihydroxytriphenylamine	Zn	4,4′,4″-trihydroxytriphenylamine	1.4	16	183
		Anthraquinone	Li metal	Anthraquinone	2.6	25	184
		Li||Tri-TEMPO	Li metal	Tri-TEMPO	3.45	33	2
		The 4,4′(5′)-bis(2-(2-methoxyethoxy)ethyl)carboxylate – tetrathiafulvalene (TTF-BMEEC)	Li metal	TTF-BMEEC	3.88	178	119
Solar rechargeable RFBs		9,10-anthraquinone-2,7-disulfonic acid (AQDS)/1,2-benzoquinone-3,5-disulfonic acid (BQDS)	AQDS	BQDS	0.55	1.15	185
		bis((3-trimethylammonio)propyl) (BTMAP) functionalized viologen (Vi) and ferrocene (Fc)	BTMAP-Vi	BTMAP-Fc	1.1	1.52	186
		Iodide/Polysulfide	S_4^{2-}/S_2^{2-}	I^-/I^{3-}	0.65	2.1	187

6. Outlook

Both semi-solid and redox targeting flow batteries have the potential to transform the energy storage landscape, offering improved performance, efficiency, and safety. As research and development efforts continue, we can expect to see these technologies being used in a range of applications, including renewable energy storage, electric vehicles, and grid stabilization. However, it is important to note that these technologies are still in the early stages of development and further research is needed to optimize their performance and reduce costs before they can be widely adopted. One of the key challenges is improving the energy density and power density of the battery. This can be achieved by optimizing the design of the RFB, developing new electrolytes, and improving the performance of the electrodes. Another challenge is to increase the efficiency of the battery. This can be achieved by reducing the resistance of the electrolyte and improving the charge and discharge rates. In addition, the use of advanced materials, such as nanomaterials, may also help to improve the efficiency of the battery. In this context, the development of LFP with advanced morphological and electronic properties could be a good direction to improve the performance of LFP based RFBs. In the case of SSRFBs, the use of LFP with optimized morphological properties, such as a high surface area and uniform particle size, can further improve the performance of the battery by increasing the electrode/electrolyte interface area and reducing mass transfer limitations. Moreover, in the case of RTFBs, the use of LFP with optimized electronic properties, such as high conductivity and low resistance, can improve the efficiency and power output of RTFBs.

Several strategies such as particle morphology and size control, surface modification, element doping and the use of prelithiation additives have been reported to enhance the properties of LFP material.[188–196] By reducing the particles to the nanoscale, the LFP cathode can provide improved power density due to the shortened pathways for Li-ion diffusion. In fact, the synthesis of nanometric LFP particles can be carried out using low temperature techniques such as solvothermal, hydrothermal, and co-

precipitation methods. However, the reduction in particles size negatively affects the volumetric energy density, since a high surface area results in poor cycling life, which could be explained by the undesirable reactions and the higher quantity of binders needed. Consequently, the fabrication of micro-nanostructure LFP materials is currently a promising approach to enhance the performances of LFP, as high-rate performance is offered by the nano-sized structure, and the high volumetric energy density and cycling performance are offered by the micro-sized structures. Innovative methods producing nano and micro-sized structures must therefore be explored to improve both rate capability and volumetric energy density of LFP cathode.

Enhancing the morphology of LFP is a crucial aspect in the development of high-performance SSFBs. However, the efficient design of SSFBs also demands a precise electrochemical model that effectively characterizes the kinetic and transport processes within these batteries. While extensive literature is available for modeling classical porous electrode batteries and redox flow batteries, the information specifically addressing SSFBs is limited. Notably, Zheng et al. [28] delved into the impact of rheological effects on the energy efficiency of aqueous SSFBs. Therefore, it becomes imperative to develop a comprehensive mathematical model that incorporates hydrodynamic and electrochemical effects in three dimensions to accurately represent the operation of flow cells.

In the context of RTFBs, establishing a theoretical computational protocol is essential for swiftly and reliably predicting the redox potentials of redox targeting molecules. This prediction aids in the screening of suitable redox mediators for RTFBs, offering an advantageous alternative to the time-consuming and expensive process of laboratory synthesis. [197–199] Density Functional Theory (DFT) emerges as a favored method for these computational studies, enabling the rapid and dependable prediction of properties like redox potential and solubility. DFT has demonstrated its efficacy in high-throughput screening of organic molecules for RFBs, achieving accuracies around 70 mV for calculated redox potentials. [152,200–203] Furthermore, the evolving landscape incorporates Machine Learning (ML) tools, which are gaining traction for similar applications. It's noteworthy that the diverse range of organic compounds results in various electronic structures, affinities, chemical bonding types, and molecular energy levels. In certain scenarios, a single theoretical approach may fall short, emphasizing the need for a comprehensive and versatile methodology. [204,205] In summary, the combination of DFT and ML is becoming instrumental in advancing the understanding and optimization of RFBs, marking a promising avenue for future research and development.

In summary, the use of $LiFePO_4$ material with optimized morphological and electronic properties in next-generation RFBs offers significant advantages in terms of energy density, stability, and safety. As technology advances, we can expect to see an increasing adoption of this technology in various applications, including renewable energy storage and grid stabilization.

7. Conclusion

In this work, recent developments of $LiFePO_4$-based flow batteries are reviewed. On the one hand, Semi-Solid Redox Flow Lithium-ion Batteries show increased potential and high energy density compared to all Vanadium RFBs (low solubility of vanadium species,) due to the high concentration of active species in a solid material than in an electrolytic solution. However, the poor fluidity and high viscosity of the active material's suspension presents a critical barrier for practical operation, therefore, more studies and formulations must be developed to overcome these drawbacks and limitations. On the other hand, the targeting-based concept has also shown improved potential and energy densities. However, several problems hindering the development of this technology such as low voltage efficiency, low power density and poor cycle stability must be addressed. The power density of redox targeting-based flow batteries depends strongly on the type and the nature of the membrane. In fact, a good selectivity of the membrane improves the capacity retention of the battery. Moreover, find soluble mediators with redox potentials targeting those of the solid active materials or a single mediator with a redox potential sufficiently close to that of this solid material kept statically in the reservoir. Finally, the use of $LiFePO_4$ with optimized morphological and electronic properties for semi-solid and redox targeting flow batteries results in a great improvement in performance, especially excellent volumetric energy density. However, gigantic efforts must be made in this field to overcome the problems and open the door for next generation redox flow batteries.

Author Contributions

Nabil El Halya, Marwa Tayoury, Mohamed Aqil, Abedelhay Aboulaich: conceptualization, data curation, writing – original draft, visualization. Rachid Amine, Fouad Ghamouss, Mohamed Makha, Jones Alami: review and editing. Mouad Dahbi: writing – review and editing, supervision.

Conflicts of interest

There are no conflicts to declare.

Acknowledgements

The authors would like to thank Office Chérifien des Phosphates (OCP S.A.) and Mohammed VI Polytechnic University for financial support. The authors also would like to acknowledge the support of the U.S. Department of Energy (DOE), Office of Energy Efficiency and Renewable Energy (EERE), Vehicle Technologies Office (VTO). Argonne National Laboratory is operated for the DOE office of Science by the UChicago Argonne, LLC, under Contract no, DE-AC02-06CH11357.

References

1 S. Maurya, S.-H. Shin, Y. Kim and S.-H. Moon, *RSC Adv.*, 2015, **5**, 37206–37230.
2 R. K. Gautam, X. Wang, A. Lashgari, S. Sinha, J. McGrath, R. Siwakoti and J. "Jimmy" Jiang, *Nat. Commun.*, 2023, **14**, 4753.
3 Y. Liang and Y. Yao, *Nat. Rev. Mater.*, 2022, **8**, 109–122.
4 D. G. Kwabi, Y. Ji and M. J. Aziz, *Chem. Rev.*, 2020, **120**, 6467–6489.
5 N. El Halya, M. Aqil, K. El Ouardi, A. Bano, A. El Bendali, L. Hdidou, R. Amine, S. Son, F. Ghamouss, D. T. Major, K. Amine, J. Alami and M. Dahbi, *Batter. Supercaps*, , DOI:10.1002/batt.202300424.
6 N. El Halya, M. Kerroumi, E. H. Elmaataouy, A. Amarray, M. Aqil, J. Alami and M. Dahbi, *RSC Adv.*, 2023, **13**, 34416–34426.
7 G. L. Soloveichik, *Chem. Rev.*, 2015, **115**, 11533–11558.
8 X. Ke, J. M. Prahl, J. I. D. Alexander, J. S. Wainright, T. A. Zawodzinski and R. F. Savinell, *Chem. Soc. Rev.*, 2018, **47**, 8721–8743.
9 W. Wang and V. Sprenkle, *Nat. Chem.*, 2016, **8**, 204–206.
10 G. Lu, Z. Wang, S. Zhang, J. Ding, J. Luo and X. Liu, *Nanoscale*, 2023, **15**, 4250–4260.
11 L. Zhang, R. Feng, W. Wang and G. Yu, *Nat. Rev. Chem.*, 2022, **6**, 524–543.
12 Y. Popat, D. Trudgeon, C. Zhang, F. C. Walsh, P. Connor and X. Li, *Chempluschem*, , DOI:10.1002/cplu.202100441.
13 I. A. Khan, A. S. Alzahrani, S. Ali, M. Mansha, M. N. Tahir, M. Khan, H. A. Qayyum and S. A. Khan, *Chem. Rec.*, , DOI:10.1002/tcr.202300171.
14 Y. Yao, J. Lei, Y. Shi, F. Ai and Y.-C. Lu, *Nat. Energy*, 2021, **6**, 582–588.

15 J. Heo, J.-Y. Han, S. Kim, S. Yuk, C. Choi, R. Kim, J.-H. Lee, A. Klassen, S.-K. Ryi and H.-T. Kim, *Nat. Commun.*, 2019, **10**, 4412.
16 C. Roth and M. Gebhard, in *Flow Batteries*, Wiley, 2023, pp. 213–227.
17 M. Duduta, B. Ho, V. C. Wood, P. Limthongkul, V. E. Brunini, W. C. Carter and Y. Chiang, *Adv. Energy Mater.*, 2011, **1**, 511–516.
18 M. Park, J. Ryu, W. Wang and J. Cho, *Nat. Rev. Mater.*, 2016, **2**, 16080.
19 K. Hatakeyama-Sato, K. Sadakuni, K. Kitagawa and K. Oyaizu, *Sci. Rep.*, 2023, **13**, 5711.
20 X. Wang, J. Chai and J. "Jimmy" Jiang, *Nano Mater. Sci.*, 2021, **3**, 17–24.
21 S. Berling, J. M. Hidalgo, N. Patil, E. García-Quismondo, J. Palma and C. Ponce de León, *J. Energy Storage*, 2023, **68**, 107620.
22 D. Reynard, M. Moghaddam, C. Wiberg, S. Sepp, P. Peljo and H. H. Girault, in *Flow Batteries*, Wiley, 2023, pp. 99–119.
23 V. E. Brunini, Y.-M. Chiang and W. C. Carter, *Electrochim. Acta*, 2012, **69**, 301–307.
24 V. E. Brunini and W. C. Carter, .
25 G. Shukla, D. del Olmo Diaz, V. Thangavel and A. A. Franco, *ACS Appl. Mater. Interfaces*, 2017, **9**, 17882–17889.
26 N. C. Hoyt, R. F. Savinell and J. S. Wainright, *Chem. Eng. Sci.*, 2016, **144**, 288–297.
27 E. Ventosa, D. Buchholz, S. Klink, C. Flox, L. G. Chagas, C. Vaalma, W. Schuhmann, S. Passerini and J. R. Morante, *Chem. Commun.*, 2015, **51**, 7298–7301.
28 Z. Li, K. C. Smith, Y. Dong, N. Baram, F. Y. Fan, J. Xie, P. Limthongkul, W. C. Carter and Y.-M. Chiang, *Phys. Chem. Chem. Phys.*, 2013, **15**, 15833.
29 C. Jia, F. Pan, Y. G. Zhu, Q. Huang, L. Lu and Q. Wang, *Sci. Adv.*, , DOI:10.1126/sciadv.1500886.
30 Q. Huang, J. Yang, C. B. Ng, C. Jia and Q. Wang, *Energy Environ. Sci.*, 2016, **9**, 917–921.
31 Y. G. Zhu, Y. Du, C. Jia, M. Zhou, L. Fan, X. Wang and Q. Wang, *J. Am. Chem. Soc.*, 2017, **139**, 6286–6289.
32 J. Li and Z.-F. Ma, *Chem*, 2019, **5**, 3–6.
33 L. Kong, C. Li, J. Jiang and M. Pecht, *Energies*, 2018, **11**, 2191.
34 D. Ouyang, M. Chen, Q. Huang, J. Weng, Z. Wang and J. Wang, *Appl. Sci.*, 2019, **9**, 2483.
35 S.-P. Chen, D. Lv, J. Chen, Y.-H. Zhang and F.-N. Shi, *Energy & Fuels*, 2022, **36**, 1232–1251.
36 J. Liang, Y. Gan and M. Yao, *J. Energy Storage*, 2023, **67**, 107546.
37 S. Ferrari, R. L. Lavall, D. Capsoni, E. Quartarone, A. Magistris, P. Mustarelli and P. Canton, *J. Phys. Chem. C*, 2010, **114**, 12598–12603.
38 L. Guo, Y. Zhang, J. Wang, L. Ma, S. Ma, Y. Zhang, E. Wang, Y. Bi, D. Wang, W. C. McKee, Y. Xu, J. Chen, Q. Zhang, C. Nan, L. Gu, P. G. Bruce and Z. Peng, *Nat. Commun.*, 2015, **6**, 7898.
39 Y. Liu, J. Liu, J. Wang, M. N. Banis, B. Xiao, A. Lushington, W. Xiao, R. Li, T.-K. Sham, G. Liang and X. Sun, *Nat. Commun.*, 2018, **9**, 929.
40 Y. Wang, C. Cui, R. Cheng, J. Wang and X. Wang, *ACS Appl. Nano Mater.*, 2023, **6**, 9124–9129.
41 J. Geng, Z. Zou, T. Wang, S. Zhang, W. Ling, X. Peng and F. Liang, *Nanotechnology*, 2023, **34**, 445403.
42 J. P. Mwizerwa, K. Xu, C. Liu, N. Zhao, Y. Li, P. Ndagijimana, Z. Chen and J. Shen, *Mater. Today Chem.*, 2023, **29**, 101483.
43 L. Zhang, Z. Zhang, Y. Song, L. Wang, H. Wang, H. Fang, H. Gao, C. Yang, A. Zhang and X. Jia, *Ionics (Kiel).*, 2023, **29**, 33–41.
44 T. Chen, B. Liu, M. Zheng and Y. Luo, *J. Energy Storage*, 2023, **57**, 106300.
45 W. Dou, M. Zheng, W. Zhang, T. Liu, F. Wang, G. Wan, Y. Liu and X. Tao, *Adv. Funct. Mater.*, , DOI:10.1002/adfm.202305161.
46 T. Qin, H. Yang, Q. Li, X. Yu and H. Li, *Ind. Chem. Mater.*, , DOI:10.1039/D3IM00089C.
47 X. Su, H. Fang, H. Yang, F. Zou, G. Li, L. Wang, H. Liao, W. Guan and X. Hu, *Carbohydr. Polym.*, 2023, **313**, 120848.
48 Z. Wang, X. Kong, Z. Fan, S. Ding, Q. Rong and Y. Su, *ChemPhysChem*, , DOI:10.1002/cphc.202300756.
49 B. Lama, A. L. Smirnova and T. R. Paudel, *ACS Appl. Energy Mater.*, 2023, **6**, 10424–10431.
50 I. D. Johnson, T. E. Ashton, E. Blagovidova, G. J. Smales, M. Lübke, P. J. Baker, S. A. Corr and J. A. Darr, *Sci. Rep.*, 2018, **8**, 4114.
51 M. J. Loveridge, M. J. Lain, I. D. Johnson, A. Roberts, S. D. Beattie, R. Dashwood, J. A. Darr and R. Bhagat, *Sci. Rep.*, 2016, **6**, 37787.
52 Y. Zhen and Y. Li, 2020, pp. 385–413.
53 E. Sánchez-Díez, E. Ventosa, M. Guarnieri, A. Trovò, C. Flox, R. Marcilla, F. Soavi, P. Mazur, E. Aranzabe and R. Ferret, *J. Power Sources*, 2021, **481**, 228804.
54 Y. Zhao, Y. Ding, Y. Li, L. Peng, H. R. Byon, J. B. Goodenough and G. Yu, *Chem. Soc. Rev.*, 2015, **44**, 7968–7996.
55 L. da Silva Lima, M. Quartier, A. Buchmayr, D. Sanjuan-Delmás, H. Laget, D. Corbisier, J. Mertens and J. Dewulf, *Sustain. Energy Technol. Assessments*, 2021, **46**, 101286.
56 J. Lee, S. Kim, K. Park, H. Koo, C. Park, Y. Park, W. B. Lee, Y. J. Lee and K. T. Lee, *Adv. Funct. Mater.*, , DOI:10.1002/adfm.202306633.
57 U. Dalal, M. Kapoor and A. Verma, *Energy & Fuels*, 2023, **37**, 13457–13466.
58 N. Shi, G. Wang, T. Mu, H. Li, R. Liu and J. Yang, *J. Mol. Liq.*, 2023, **376**, 121401.
59 M. He, M. Guan, R. Zhan, K. Zhou, H. Fu, X. Wang, F. Zhong, M. Ding and C. Jia, *Chem. – An Asian J.*, , DOI:10.1002/asia.202201152.
60 J. Ye, J. Liu, C. Zheng, T. Sun, S. Yu and H. Li, *Sustain. Mater. Technol.*, 2023, **35**, e00550.
61 Z. Wang, J. Ren, J. Sun, Y. Li, Z. Guo, B. Liu, X. Fan and T. Zhao, *Chem. Eng. J.*, 2023, **474**, 145621.
62 A. Fetyan, B. P. Benetho and M. O. Bamgbopa, *J. Energy Chem.*, 2023, **81**, 64–70.
63 R. Tan, A. Wang, C. Ye, J. Li, D. Liu, B. P. Darwich, L. Petit, Z. Fan, T. Wong, A. Alvarez-Fernandez, M. Furedi, S. Guldin, C.

E. Breakwell, P. A. A. Klusener, A. R. Kucernak, K. E. Jelfs, N. B. McKeown and Q. Song, *Adv. Sci.*, , DOI:10.1002/advs.202206888.
64 J. Qian, S. Cai, J. Hu, C. Wang and G. Li, *Ind. Eng. Chem. Res.*, 2023, **62**, 2719–2728.
65 X. Liu, P. Zhang, J. Yang, J. Li and F. Chu, *Int. J. Heat Mass Transf.*, 2023, **215**, 124382.
66 H. Fu, X. Bao, M. He, J. Xu, Z. Miao, M. Ding, J. Liu and C. Jia, *J. Power Sources*, 2023, **556**, 232443.
67 M. van der Heijden, M. Kroese, Z. Borneman and A. Forner-Cuenca, *Adv. Mater. Technol.*, , DOI:10.1002/admt.202300611.
68 Q. Ma, W. Fu, L. Zhao, Z. Chen, H. Su and Q. Xu, *Energy*, 2023, **265**, 126291.
69 T. Sun, Y. Fan, X. Liu, J. Yang, J. Fu, Z. Tan and F. Chu, *Chem. Eng. J.*, 2023, **462**, 142197.
70 G. Dey, S. Saifi, H. Sharma, M. Kumar and A. Aijaz, *ACS Appl. Nano Mater.*, 2023, **6**, 8192–8201.
71 J. Ji, C. Noh, M. Shin, S. Oh, Y. Chung, Y. Kwon and D.-H. Kim, *Appl. Surf. Sci.*, 2023, **611**, 155665.
72 P.-J. Alphonse, M. Taş and G. Elden, *Fuel*, 2023, **333**, 126198.
73 L. Qiao, M. Fang, S. Liu, H. Zhang and X. Ma, *Chem. Eng. J.*, 2022, **434**, 134588.
74 M. Ulaganathan, V. Aravindan, Q. Yan, S. Madhavi, M. Skyllas-Kazacos and T. M. Lim, *Adv. Mater. Interfaces*, , DOI:10.1002/admi.201500309.
75 Y. Guo, J. Huang and J.-K. Feng, *J. Ind. Eng. Chem.*, 2023, **118**, 33–43.
76 A. Zhou, X. Shao, D. Li, Y. Du, Y. Zhang, L. Cao and J. Yang, *J. Power Sources*, 2024, **591**, 233890.
77 P. Bavdane, S. Sreenath, D. Y. Nikumbe, B. Bhatt, C. M. Pawar, V. Dave and R. K. Nagarale, *RSC Appl. Polym.*, , DOI:10.1039/D3LP00152K.
78 M. Pahlevaninezhad, E. E. Miller, L. Yang, L. S. Prophet, A. Singh, T. Storwick, M. Pahlevani, M. A. Pope and E. P. L. Roberts, *ACS Appl. Energy Mater.*, 2023, **6**, 6505–6517.
79 M. Mara Ikhsan, S. Abbas, S.-Y. Choi, X. H. Do, H. Y. Ha, A. Bentien, K. Azizi, H. A. Hjuler and D. Henkensmeier, *Mater. Today Chem.*, 2023, **34**, 101830.
80 H. Doğan, M. Taş, T. Meşeli, G. Elden and G. GENC, *ACS Omega*, 2023, **8**, 34310–34327.
81 Q. Ma, W. Fu, H. Shi, Z. Chen, H. Su and Q. Xu, *J. Energy Storage*, 2023, **74**, 109392.
82 J. Xu, Q. Ma, L. Xing, H. Li, P. Leung, W. Yang, H. Su and Q. Xu, *J. Power Sources*, 2020, **449**, 227491.
83 W. Lee, B. W. Kwon, M. Jung, D. Serhiichuk, D. Henkensmeier and Y. Kwon, *J. Power Sources*, 2019, **439**, 227079.
84 D. Kim, Y. Kim, Y. Lee and J. Jeon, *Int. J. Hydrogen Energy*, 2019, **44**, 12024–12032.
85 M. Hasnat Hossain, N. Abdullah, S. Rahman and M. Amran Mohd Radzi, *Mater. Today Proc.*, , DOI:10.1016/j.matpr.2023.01.396.
86 P. K. Leung, M. R. Mohamed, A. A. Shah, Q. Xu and M. B. Conde-Duran, *J. Power Sources*, 2015, **274**, 651–658.
87 S. Sankarasubramanian, Y. Zhang and V. Ramani, *Sustain. Energy Fuels*, 2019, **3**, 2417–2425.
88 S. Smith, I. Firdous, Q. Wang, S. Esmalla and W. A. Daoud, *Electrochim. Acta*, 2019, **328**, 135019.
89 S. Yun, J. Parrondo and V. Ramani, *Chempluschem*, 2015, **80**, 412–421.
90 S. V. Modak, W. Shen, S. Singh, D. Herrera, F. Oudeif, B. R. Goldsmith, X. Huan and D. G. Kwabi, *Nat. Commun.*, 2023, **14**, 3602.
91 X.-L. Lv, P. T. Sullivan, W. Li, H.-C. Fu, R. Jacobs, C.-J. Chen, D. Morgan, S. Jin and D. Feng, *Nat. Energy*, 2023, **8**, 1109–1118.
92 B. Ambrose, R. Naresh, M. Kathiresan, M. Ulaganathan and P. Ragupathy, *Energy Technol.*, , DOI:10.1002/ente.202201046.
93 W. Lee, K. In Shim, G. Park, J. W. Han and Y. Kwon, *Chem. Eng. J.*, 2023, **464**, 142661.
94 K. Peng, Y. Li, G. Tang, Y. Liu, Z. Yang and T. Xu, *Energy Environ. Sci.*, 2023, **16**, 430–437.
95 A. Ramar, F.-M. Wang, R. Foeng and R. Hsing, *J. Power Sources*, 2023, **558**, 232611.
96 M. Pan, M. Shao and Z. Jin, *SmartMat*, , DOI:10.1002/smm2.1198.
97 J. Kim, Y. Kim, J. Yoo, G. Kwon, Y. Ko and K. Kang, *Nat. Rev. Mater.*, 2022, **8**, 54–70.
98 T. Kong, J. Liu, X. Zhou, J. Xu, Y. Xie, J. Chen, X. Li and Y. Wang, *Angew. Chemie Int. Ed.*, , DOI:10.1002/anie.202214819.
99 A. Permatasari, M. Mara Ikhsan, D. Henkensmeier and Y. Kwon, *J. Ind. Eng. Chem.*, 2023, **122**, 264–273.
100 R. Walser-Kuntz, Y. Yan, M. Sigman and M. S. Sanford, *Acc. Chem. Res.*, 2023, **56**, 1239–1250.
101 N.-U. Seo, K. Kim, J. Yeo, S. J. Kwak, Y. Kim, H. Kim, M. S. Kim, J. Choi, Y. S. Jung, J. Chae, J. Chang and J. H. Yang, *J. Mater. Chem. A*, 2023, **11**, 18953–18963.
102 R. Duke, V. Bhat, P. Sornberger, S. A. Odom and C. Risko, *Digit. Discov.*, 2023, **2**, 1152–1162.
103 Y. Zheng, Á. P. Ramos, H. Wang, G. Álvarez, A. Ridruejo and J. Peng, *Mater. Today Energy*, 2023, **34**, 101286.
104 T. Janoschka, N. Martin, U. Martin, C. Friebe, S. Morgenstern, H. Hiller, M. D. Hager and U. S. Schubert, *Nature*, 2015, **527**, 78–81.
105 M. Aqil, A. Aqil, F. Ouhib, A. El Idrissi, C. Detrembleur and C. Jérôme, *RSC Adv.*, 2015, **5**, 85035–85038.
106 K. Lin, R. Gómez-Bombarelli, E. S. Beh, L. Tong, Q. Chen, A. Valle, A. Aspuru-Guzik, M. J. Aziz and R. G. Gordon, *Nat. Energy*, 2016, **1**, 16102.
107 X. Li, P. Gao, Y.-Y. Lai, J. D. Bazak, A. Hollas, H.-Y. Lin, V. Murugesan, S. Zhang, C.-F. Cheng, W.-Y. Tung, Y.-T. Lai, R. Feng, J. Wang, C.-L. Wang, W. Wang and Y. Zhu, *Nat. Energy*, 2021, **6**, 873–881.
108 W. Yan, C. Wang, J. Tian, G. Zhu, L. Ma, Y. Wang, R. Chen, Y. Hu, L. Wang, T. Chen, J. Ma and Z. Jin, *Nat. Commun.*, 2019, **10**, 2513.
109 Y. Y. Lai, X. Li and Y. Zhu, *ACS Appl. Polym. Mater.*, 2020, **2**, 113–128.
110 M. E. Carrington, K. Sokołowski, E. Jónsson, E. W. Zhao, A. M. Graf, I. Temprano, J. A. McCune, C. P. Grey and O. A.

Scherman, *Nature*, 2023, **623**, 949–955.
111 E. Schröter, C. Stolze, J. Meyer, M. D. Hager and U. S. Schubert, *ChemSusChem*, , DOI:10.1002/cssc.202300296.
112 S. Huang, H. Zhang, M. Salla, J. Zhuang, Y. Zhi, X. Wang and Q. Wang, *Nat. Commun.*, 2022, **13**, 4746.
113 M. Aqil, A. Aqil, F. Ouhib, A. El Idrissi, M. Dahbi, C. Detrembleur and C. Jérôme, *Eur. Polym. J.*, 2021, **152**, 110453.
114 Q. Huang and Q. Wang, *Chempluschem*, 2015, **80**, 312–322.
115 Y. Wang, Z. Niu, Q. Zheng, C. Zhang, J. Ye, G. Dai, Y. Zhao and X. Zhang, *Sci. Rep.*, 2018, **8**, 5740.
116 Z. Li and Y.-C. Lu, *Nat. Energy*, 2021, **6**, 517–528.
117 J. S. Shamie, C. Liu, L. L. Shaw and V. L. Sprenkle, *Sci. Rep.*, 2015, **5**, 11215.
118 B. Li, Z. Nie, M. Vijayakumar, G. Li, J. Liu, V. Sprenkle and W. Wang, *Nat. Commun.*, 2015, **6**, 6303.
119 N. Chen, D. Chen, J. Wu, Y. Lai and D. Chen, *Chem. Eng. J.*, 2023, **462**, 141996.
120 J. Park, M. Kim, J. Choi, S. Lee, J. Kim, D. Han, H. Jang and M. Park, *Chem. – An Asian J.*, , DOI:10.1002/asia.202201052.
121 W. D. McCulloch, M. Yu and Y. Wu, *ACS Energy Lett.*, 2016, **1**, 578–582.
122 W. Li, J. Zheng, B. Hu, H.-C. Fu, M. Hu, A. Veyssal, Y. Zhao, J.-H. He, T. L. Liu, A. Ho-Baillie and S. Jin, *Nat. Mater.*, 2020, **19**, 1326–1331.
123 H.-C. Fu, W. Li, Y. Yang, C.-H. Lin, A. Veyssal, J.-H. He and S. Jin, *Nat. Commun.*, 2021, **12**, 156.
124 J. R. McKone, F. J. DiSalvo and H. D. Abruña, *J. Mater. Chem. A*, 2017, **5**, 5362–5372.
125 G. Rodriguez-Garcia, H.-C. Fu, P. Sullivan, C.-J. Chen, Z. Song, J. Chen, Y. Yan, D. Feng, S. Jin and I. Celik, *J. Clean. Prod.*, 2023, **397**, 136533.
126 N. Ra, A. Ghosh and A. Bhattacharjee, *Energy Convers. Manag.*, 2023, **281**, 116851.
127 L. Cao, M. Skyllas-Kazacos and D. Wang, *Adv. Sustain. Syst.*, , DOI:10.1002/adsu.201800031.
128 K. Wedege, D. Bae, W. A. Smith, A. Mendes and A. Bentien, *J. Phys. Chem. C*, 2018, **122**, 25729–25740.
129 J. Azevedo, T. Seipp, J. Burfeind, C. Sousa, A. Bentien, J. P. Araújo and A. Mendes, *Nano Energy*, 2016, **22**, 396–405.
130 W. Li and S. Jin, *Acc. Chem. Res.*, 2020, **53**, 2611–2621.
131 B. Xue, X. Wu, Y. Ren, Y. Guo and C. Zhang, *J. Power Sources*, 2023, **563**, 232816.
132 D. Perez-Antolin, W. Schuhmann, J. Palma and E. Ventosa, *J. Power Sources*, 2022, **536**, 231480.
133 J. J. Biendicho, C. Flox, L. Sanz and J. R. Morante, *ChemSusChem*, 2016, **9**, 1938–1944.
134 H. Chen and Y. Lu, *Adv. Energy Mater.*, , DOI:10.1002/aenm.201502183.
135 H. Chen, N.-C. Lai and Y.-C. Lu, *Chem. Mater.*, 2017, **29**, 7533–7542.
136 X. Zhang, P. Zhang and H. Chen, *ChemSusChem*, 2021, **14**, 1913–1920.
137 T. M. Narayanan, Y. G. Zhu, E. Gençer, G. McKinley and Y. Shao-Horn, *Joule*, 2021, **5**, 2934–2954.
138 X. Xing, Q. Liu, J. Li, Z. Han, B. Wang and J. P. Lemmon, *Chem. Commun.*, 2019, **55**, 14214–14217.
139 K. Dong, S. Wang and J. Yu, *RSC Adv.*, 2014, **4**, 47517–47520.
140 F. Soavi, A. Brilloni, F. De Giorgio and F. Poli, *Curr. Opin. Chem. Eng.*, 2022, **37**, 100835.
141 R. Yan and Q. Wang, *Adv. Mater.*, , DOI:10.1002/adma.201802406.
142 E. Schröter, C. Stolze, A. Saal, K. Schreyer, M. D. Hager and U. S. Schubert, *ACS Appl. Mater. Interfaces*, 2022, **14**, 6638–6648.
143 F. Pan, J. Yang, Q. Huang, X. Wang, H. Huang and Q. Wang, *Adv. Energy Mater.*, , DOI:10.1002/aenm.201400567.
144 Q. Huang, H. Li, M. Grätzel and Q. Wang, *Phys. Chem. Chem. Phys.*, 2013, **15**, 1793–1797.
145 J. Yu, L. Fan, R. Yan, M. Zhou and Q. Wang, *ACS Energy Lett.*, 2018, **3**, 2314–2320.
146 C. M. Wong and C. S. Sevov, *ACS Energy Lett.*, 2021, 1271–1279.
147 X. Wang, M. Zhou, F. Zhang, H. Zhang and Q. Wang, *Curr. Opin. Electrochem.*, 2021, **29**, 100743.
148 Y. Chen, M. Zhou, Y. Xia, X. Wang, Y. Liu, Y. Yao, H. Zhang, Y. Li, S. Lu, W. Qin, X. Wu and Q. Wang, *Joule*, 2019, **3**, 2255–2267.
149 L. Fan, C. Jia, Y. G. Zhu and Q. Wang, *ACS Energy Lett.*, 2017, **2**, 615–621.
150 G. Lee, C. M. Wong and C. S. Sevov, *ACS Energy Lett.*, 2022, **7**, 3337–3344.
151 H. Zhang, Q. Huang, X. Xia, Y. Shi, Y.-M. Shen, J. Xu, Z. Chen and J. Cao, *J. Mater. Chem. A*, 2022, **10**, 6740–6747.
152 N. Rahbani, P. de Silva and E. Baudrin, *ChemSusChem*, , DOI:10.1002/cssc.202300482.
153 E. Ventosa, O. Amedu and W. Schuhmann, *ACS Appl. Energy Mater.*, 2018, acsaem.8b01418.
154 K. Wada, K. Sakaushi, S. Sasaki and H. Nishihara, *Angew. Chemie Int. Ed.*, 2018, **57**, 8886–8890.
155 J. Li, D. Zhou, W. Qiu, Y. Shi, J.-J. Yang, S. Chen, Q. Wang and H. Pan, *Sci. Rep.*, 2018, **8**, 622.
156 J. Yan, J. Wang, H. Liu, Z. Bakenov, D. Gosselink and P. Chen, *J. Power Sources*, 2012, **216**, 222–226.
157 N. Yesibolati, N. Umirov, A. Koishybay, M. Omarova, I. Kurmanbayeva, Y. Zhang, Y. Zhao and Z. Bakenov, *Electrochim. Acta*, 2015, **152**, 505–511.
158 J. Fu, Z. P. Cano, M. G. Park, A. Yu, M. Fowler and Z. Chen, *Adv. Mater.*, , DOI:10.1002/adma.201604685.
159 H. Chen, Y. Liu, X. Zhang, Q. Lan, Y. Chu, Y. Li and Q. Wu, *J. Power Sources*, 2021, **485**, 229319.
160 Y. Hu, S. Cheng, P. Liu, J. Zhang, Q. Duan, H. Xiao, J. Sun and Q. Wang, *Fire Technol.*, 2023, **59**, 1199–1220.
161 R. Wang, L. Yang, J. Li, S. Pan, F. Zhang, H. Zhang and S. Zhang, *Nano Energy*, 2023, **108**, 108174.
162 D. Perez-Antolin, R. Trócoli, J. Palma and E. Ventosa, *J. Power Sources*, 2020, **480**, 228839.
163 K. Yang, S. Xiong and H. Zhang, *J. Power Sources*, 2022, **531**, 231315.
164 F. Zhang, M. Gao, S. Huang, H. Zhang, X. Wang, L. Liu, M. Han and Q. Wang, *Adv. Mater.*, , DOI:10.1002/adma.202104562.

165 Q. Wang, S. M. Zakeeruddin, D. Wang, I. Exnar and M. Grätzel, *Angew. Chemie*, 2006, **118**, 8377–8380.
166 J. Noack, N. Roznyatovskaya, T. Herr and P. Fischer, *Angew. Chemie Int. Ed.*, 2015, **54**, 9776–9809.
167 C. Jia, Q. Liu, C.-J. Sun, F. Yang, Y. Ren, S. M. Heald, Y. Liu, Z.-F. Li, W. Lu and J. Xie, *ACS Appl. Mater. Interfaces*, 2014, **6**, 17920–17925.
168 Y. Orikasa, T. Maeda, Y. Koyama, H. Murayama, K. Fukuda, H. Tanida, H. Arai, E. Matsubara, Y. Uchimoto and Z. Ogumi, *Chem. Mater.*, 2013, **25**, 1032–1039.
169 X. Wei, G.-G. Xia, B. Kirby, E. Thomsen, B. Li, Z. Nie, G. G. Graff, J. Liu, V. Sprenkle and W. Wang, *J. Electrochem. Soc.*, 2016, **163**, A5150–A5153.
170 Z. Li, G. Weng, Q. Zou, G. Cong and Y.-C. Lu, *Nano Energy*, 2016, **30**, 283–292.
171 J. Lei, Y. Zhang, Y. Yao, Y. Shi, K. L. Leung, J. Fan and Y.-C. Lu, *Nat. Energy*, , DOI:10.1038/s41560-023-01370-0.
172 J. F. Vivo-Vilches, A. Nadeina, N. Rahbani, V. Seznec, D. Larcher and E. Baudrin, *J. Power Sources*, 2021, **488**, 229387.
173 M. Zhou, Q. Huang, T. N. Pham Truong, J. Ghilane, Y. G. Zhu, C. Jia, R. Yan, L. Fan, H. Randriamahazaka and Q. Wang, *Chem*, 2017, **3**, 1036–1049.
174 D. Gupta, Y. Zhang, Z. Nie, J. Wang and G. M. Koenig Jr, *Chem. Eng. Sci.*, 2022, **251**, 117443.
175 H. Nariyama, S. Ito, Y. Okada, Y. Inatomi, K. Ichikawa, Y. Masumoto and M. Fujimoto, *Electrochim. Acta*, 2022, **409**, 139915.
176 D. M. Hall, J. Grenier, T. S. Duffy and S. N. Lvov, *J. Electrochem. Soc.*, 2020, **167**, 110536.
177 F. J. Vázquez Galván, *Thesis*.
178 X. Huo, X. Shi, Y. Bai, Y. Zeng and L. An, *Cell Reports Phys. Sci.*, 2024, **5**, 101782.
179 B. Huskinson, M. P. Marshak, C. Suh, S. Er, M. R. Gerhardt, C. J. Galvin, X. Chen, A. Aspuru-Guzik, R. G. Gordon and M. J. Aziz, *Nature*, 2014, **505**, 195–198.
180 B. Yang, L. Hoober-Burkhardt, F. Wang, G. K. Surya Prakash and S. R. Narayanan, *J. Electrochem. Soc.*, 2014, **161**, A1371–A1380.
181 B. Liu, C. W. Tang, H. Jiang, G. Jia and T. Zhao, *J. Power Sources*, 2020, **477**, 228985.
182 G. Nikiforidis and W. A. Daoud, *Electrochim. Acta*, 2014, **141**, 255–262.
183 X. Wang, W. Tang and K. P. Loh, *ACS Appl. Energy Mater.*, 2021, **4**, 3612–3621.
184 W. Wang, W. Xu, L. Cosimbescu, D. Choi, L. Li and Z. Yang, *Chem. Commun.*, 2012, **48**, 6669.
185 W. Li, H. Fu, L. Li, M. Cabán-Acevedo, J. He and S. Jin, *Angew. Chemie*, 2016, **128**, 13298–13302.
186 W. Li, E. Kerr, M. Goulet, H. Fu, Y. Zhao, Y. Yang, A. Veyssal, J. He, R. G. Gordon, M. J. Aziz and S. Jin, *Adv. Energy Mater.*, , DOI:10.1002/aenm.201900918.
187 M. A. Mahmoudzadeh, A. R. Usagocar, J. Giorgio, D. L. Officer, G. Wallace and J. D. W. Madden, *ECS Trans.*, 2016, **72**, 23–31.
188 M. Cao, Z. Liu, X. Zhang, L. Yang, S. Xu, S. Weng, S. Zhang, X. Li, Y. Li, T. Liu, Y. Gao, X. Wang, Z. Wang and L. Chen, *Adv. Funct. Mater.*, , DOI:10.1002/adfm.202210032.
189 Y. Zhao, W. Li, J. Wu, X. Zhou and Z. Liu, *Energy Technol.*, , DOI:10.1002/ente.202300344.
190 H. Zhang, J. Cheng, H. Liu, D. Li, Z. Zeng, Y. Li, F. Ji, Y. Guo, Y. Wei, S. Zhang, T. Bai, X. Xu, R. Peng, J. Lu and L. Ci, *Adv. Energy Mater.*, , DOI:10.1002/aenm.202300466.
191 Q. Xiao, Y. Li, Y. Zhang and S. Huang, *Energy Technol.*, , DOI:10.1002/ente.202300361.
192 Y. Li, Z. Fan, Z. Peng, Z. Xu, X. Zhang, J. Zhou, X. Lin, Z. Wu, E. Zhao and R. Zeng, *EcoMat*, , DOI:10.1002/eom2.12415.
193 M. A. M. M. AL-SAMET and E. Burgaz, *J. Alloys Compd.*, 2023, **947**, 169680.
194 W. Xu, D. Liu, X. Liu, D. Wang, L. He and Z. Zhao, *Desalination*, 2023, **546**, 116188.
195 S. Wang and F. Wang, *J. Mol. Graph. Model.*, 2023, **125**, 108604.
196 J. Wang, M. Wang, Y. Liang, X. Liu, Y. Cui, S. Xing, H. Tao, B. Song and Z. Zhang, *Phys. B Condens. Matter*, 2023, **648**, 414437.
197 Y. Ding, C. Zhang, L. Zhang, Y. Zhou and G. Yu, *Chem. Soc. Rev.*, 2018, **47**, 69–103.
198 J. Wu, *AIChE J.*, 2006, **52**, 1169–1193.
199 A. Zaichenko, A. J. Achazi, S. Kunz, H. A. Wegner, J. Janek and D. Mollenhauer, *Prog. Energy*, 2024, **6**, 012001.
200 S. Er, C. Suh, M. P. Marshak and A. Aspuru-Guzik, *Chem. Sci.*, 2015, **6**, 885–893.
201 Y. Moon and Y.-K. Han, *Curr. Appl. Phys.*, 2016, **16**, 939–943.
202 Q. Zhang, A. Khetan, E. Sorkun, F. Niu, A. Loss, I. Pucher and S. Er, *Energy Storage Mater.*, 2022, **47**, 167–177.
203 R. P. Fornari and P. de Silva, *WIREs Comput. Mol. Sci.*, , DOI:10.1002/wcms.1495.
204 J. L. Borioni, M. Puiatti, D. M. A. Vera and A. B. Pierini, *Phys. Chem. Chem. Phys.*, 2017, **19**, 9189–9198.
205 M. Isegawa, F. Neese and D. A. Pantazis, *J. Chem. Theory Comput.*, 2016, **12**, 2272–2284.